This is the author's version (manuscript) of the work that was accepted for publication in
Science of the Total Environment
The Version of Record is available online at https://doi.org/10.1016/j.scitotenv.2022.153232

TROPOspheric Monitoring Instrument observations of total column water vapour: algorithm and validation

Ka Lok Chan[a,b,*], Jian Xu[a,c], Sander Slijkhuis[a], Pieter Valks[a], Diego Loyola[a]

[a] *Remote Sensing Technology Institute, German Aerospace Center (DLR), Oberpfaffenhofen, Germany*
[b] *Rutherford Appleton Laboratory Space, Harwell Oxford, United Kingdom*
[c] *National Space Science Center, Chinese Academy of Sciences, Beijing, China*

Abstract

In this paper, we present the total column water vapour (TCWV) retrieval for the TROPOspheric Monitoring Instrument (TROPOMI) observations in the visible blue spectral band. The TROPOMI TCWV algorithm is being optimized and validated in the framework of the Sentinel 5 Precursor Product Algorithm Laboratory (S5P-PAL) project from the European Space Agency (ESA). The retrieval was first developed to retrieve TCWV from the Global Ozone Monitoring Experiment 2 (GOME-2). We have optimized the settings of the retrieval to adapt it for TROPOMI observations. The TROPOMI TCWV algorithm follows the typical two step approach, using spectral fit retrieval of slant columns, and conversion of the slant columns to vertical columns using air mass factors (AMFs). An iterative optimization algorithm is developed to dynamically find the optimal a priori water vapour profile for the AMF calculation. Further optimizations on the spectral retrieval, air mass factor calculations as well as a new surface albedo retrieval approach are implemented.

The TCWV retrieval algorithm is applied to TROPOMI observations from May 2018 to May 2021. The results are validated by comparing them to ERA5 reanalysis data, GOME-2, MODerate resolution Imaging Spectroradiometer (MODIS) and Special Sensor Microwave Imager Sounder (SSMIS) satellite observations. TCWV derived from TROPOMI observations agree well with the other data sets with Pearson correlation coefficient (R) ranging from 0.96 to 0.99. The mean bias between TROPOMI and ERA5 data is -1.24 $\mathrm{kg\,m^{-2}}$ for measurements over land and 0.73 $\mathrm{kg\,m^{-2}}$ for measurements over water. The comparison to MODIS observations show similar results with small dry bias of 1.51,$\mathrm{kg\,m^{-2}}$ for measurements over land and a small wet bias of 1.25 $\mathrm{kg\,m^{-2}}$ for measurements over water. Slightly larger dry bias of 1.98 $\mathrm{kg\,m^{-2}}$ for measurements over land and 1.74 $\mathrm{kg\,m^{-2}}$ for measurements over water are found when compared to GOME-2 oberations. Compared to SSMIS data over water, TROPOMI observations are bias low by 3.25 $\mathrm{kg\,m^{-2}}$. The small discrepancies found between TROPOMI and reference data sets are related to the differences in measurement technique, measurement time, surface albedo issue, as well as cloud and aerosol contamination. This study demonstrates that the algorithm can provide stable and consistent results on a global scale and can be applied to generate operational TCWV products from TROPOMI and the forthcoming Copernicus missions Sentinel-4 and Sentinel-5. We have also demonstrated the capability of retrieving fine scale water vapour structures in a case study over the Amazon. This indicates that the TROPOMI data set is also useful for local and regional climate studies.

Keywords: water vapour, TROPOMI, Sentinel-5P, GOME-2, MODIS, SSMIS

*Corresponding author
Email address: Ka.Chan@dlr.de (Ka Lok Chan)

1. introduction

Water vapour is one of the major components in the atmosphere with strong impacts on the earth's climate and weather. Water vapour absorbs radiation in the infrared spectral range and its abundance in the atmosphere, making it the most important natural greenhouse gas (Clough and Iacono, 1995; Kiehl and Trenberth, 1997). Notwithstanding this importance, the role of water vapour in climate and its reactions to climate change are still difficult to assess. On the one hand, the atmospheric water vapour content of the atmosphere is expected to rise with increasing atmospheric temperature (Trenberth and Stepaniak, 2003; Hodnebrog et al., 2019), which further amplifies the warming effect (Colman, 2003; Soden et al., 2005; Soden and Held, 2006; Evan et al., 2015). On the other hand, higher water vapour content in the atmosphere could also enhance cloud formation, where clouds are known to have cooling effect to the Earth's surface (Bellomo et al., 2014; Brown et al., 2016). Therefore, the warming or cooling effect of increasing water vapour amounts in the atmosphere is still not well understood (Boucher et al., 2013). The warming of atmosphere would also intensify the horizontal transport of atmospheric water vapour as well as its spatio-temporal patterns (Schneider et al., 2010; Lavers et al., 2015). In addition, the lifetime of atmopsheric water vapour is rather short compared to other greenhouse gases, hence it has a very strong spatio-temporal variability making the assessment more difficult. Accurate measurements of water vapour on a global scale are therefore necessary for the investigation and evaluation of its interactions with the earth's climate (Hartmann et al., 2013).

Satellite remote sensing is an essential tool for the monitoring of atmospheric water vapour on global scale. Satellite observations of water vapour can be conducted in various electromagnetic spectral bands, i.e, microwave, infrared and visible bands (Kaufman and Gao, 1992; Bauer and Schlüssel, 1993; Noël et al., 1999, 2004; Li et al., 2006; Wagner et al., 2006; Pougatchev et al., 2009; Wang et al., 2014; Grossi et al., 2015). Although water vapour absorption in the visible wavelength band is a few orders of magnitude lower than at longer wavelengths, satellite observations of water vapour in the visible band have certain advantages compared to measurements at longer wavelengths. Surface albedo in the visible blue band over ocean is higher than that in the infrared, and yields better sensitivity to the lower troposphere where most of the water vapour resides. In addition, a non-linearity absorption correction is not required for measurements in the visible blue band, as the absorption at this wavelength band is rather low.

Spectroscopic observations of earthshine radiance in the ultraviolet (UV), visible (VIS) and near infrared (NIR) bands have long been conducted since the Global Ozone Monitoring Experiment (GOME) satellite mission was launched in 1995 (Burrows et al., 1999). Together with follow up missions such as the SCanning Imaging Absorption SpectroMeter for Atmospheric CHartographY (SCIAMACHY) (Bovensmann et al., 1999), Global Ozone Monitoring Experiment 2 (GOME-2) (Callies et al., 2000), and Ozone Monitoring Instrument (OMI) (Levelt et al., 2006) these observations provide a global record of earthshine radiance in the UV, VIS and NIR (UVN) spectral range for more than 25 years. The recent TROPOspheric Monitoring Instrument

(TROPOMI) satellite borne spectrometer (Veefkind et al., 2012) on board the European Space Agency (ESA) Sentinel 5 Precursor (S5P) satellite provides daily global observations of earthshine radiance in the UVN range with much finer spatial resolution ($3.5 \times 7.0\,\mathrm{km}^2$ and $3.5 \times 5.5\,\mathrm{km}^2$ after August 2019) compared to its predecessors. TROPOMI and the upcoming Sentinel 5 (S5) missions will provide indispensable global observations of earthshine radiance in the UVN range in the next decade. However, water vapour is still not yet one of the official TROPOMI operational products. In order to fully exploit the potential of TROPOMI observations, we have developed the total column water vapour (TCWV) retrieval algorithm for TROPOMI within the European Space Agency's (ESA's) Sentinel 5 Precursor Product Algorithm Laboratory (S5P-PAL) framework. The TROPOMI water vapour algorithm is based on the GOME-2 total column water vapour retrieval with optimizations on spectral analysis, air mass factor calculations and new surface albedo retrieval approach.

The objective of this paper is to present the TROPOMI TCWV retrieval algorithm which is based on the experience from GOME-2 and to produce a consistent TCWV data set. This paper presents the details of the TROPOMI TCWV retrieval algorithm and validation against external data sets. The manuscript is organized as follows. The description of the TROPOMI instrument and other data sets used for validation are presented in Section 2. Section 3 describes the TROPOMI TCWV retrieval algorithm. The results of validation against external data sets results are shown in Section 4. Section 5 presents an example of using the high spatial resolution TROPOMI TCWV data to observe fine scale features of water vapour. Section 6 summarizes the study.

2. Instruments and data sets

In this section, the TROPOMI instrument and its corresponding products used in the retrieval are described. In addition, TCWV validation data sets measured by other satellite instruments and the ERA5 reanalysis data are presented.

2.1. TROPOMI measurements

TROPOspheric Monitoring Instrument (TROPOMI) is a passive nadir viewing satellite borne push-broom grating imaging spectrometer on board the Copernicus Sentinel 5 Precursor (S5P) satellite. The satellite was launched on 13^{th} October 2017 and orbits on sun-synchronous orbit at an altitude of $\sim$824 km with local equator overpass time of 13:30 LT (local time) on ascending node. The instrument has 8 spectral bands covering ultraviolet (UV), visible (Vis), near infrared (NIR) and short-wavelength infrared (SWIR). The instrument takes measurements at 450 positions across the orbital track which cover a swath width of approximately 2600 km, providing daily global coverage observations. The spatial resolution of the instrument was 3.5 km (across-track) $\times$ 7.0 km (alongtrack) for measurements taken before 6^{th} August 2019 and 3.5 km (across-track) $\times$ 5.5 km (alongtrack) after 6^{th} August 2019. The TCWV retrieval utilizes spectral observations in band 4 (400 - 495 nm) with typical spectral resolution of 0.54 nm. The description of the spectral calibration of the TROPOMI instruments can be found in Kleipool et al. (2018); Ludewig et al. (2020). A more detailed description of the TROPOMI instrument can be found in Veefkind et al. (2012).

The first step of TROPOMI data processing is the conversion of the detector signal (level 0 data) to geolocated and radiometric calibrated radiance and irradiance data (level 1B data). The operational TROPOMI level 1B processor has been developed by the Royal Netherlands Meteorological Institute (Koninklijk Nederlands Meteorologisch Instituut, KNMI). It uses instrument calibration key data to convert level 0 to level 1B data. The calibration key data includes information such as detector dark current, offset, non-linearity, instrument slit response function (ISRF), etc, which are acquired from the pre-flight on-ground calibration. More details of the instrument calibration can be found in Kleipool et al. (2018). The calibrated level 1B data is then used for the retrieval of cloud information and TCWV.

2.2. ERA5 reanalysis data

ERA5 (ECMWF Reanalysis version 5) is a global atmosphere, land surface and ocean waves reanalysis data set produced by the European Center for Medium-Range Weather Forecasts (ECMWF) as part of Copernicus Climate Change Services (C3S). The ERA5 reanalysis data covers a long time period since 1979, providing consistent data on a global scale for the analysis of long term variation of water vapour in the atmosphere. The reanalysis data is produced with a data assimilation scheme which combined various measurements, including radiosonde, satellite and ground based remote sensing observations, as prior information from model forecasts (Hersbach et al., 2020). The original TCWV reanalysis data is in a spatial resolution of $\sim$31 km and temporal resolution of 1 hour. The data is then transformed to the latitude longitude (LL) coordinate system with a horizontal resolution of $0.25° \times 0.25°$ through the Copernicus Climate Change Service. A more detailed description of ERA5 reanalysis data can be found in Hersbach et al. (2020). The ERA5 TCWV data is spatio-temporally interpolated to the measurement time and location of each individual TROPOMI pixel for comparison and subsequent processing. The ERA5 reanalysis data is publicly available through the Copernicus Climate Change Services (`https://cds.climate.copernicus.eu/`).

2.3. GOME-2 TCWV product

The GOME-2 water vapour product (Grossi et al., 2015) is used as reference to validate the TROPOMI TCWV data set. Data from both GOME-2 instruments on board the MetOp-A and MetOp-B satellites are used. The MetOp satellites orbit at an altitude of $\sim$820 km on sun-synchronous orbits with a repeat cycle of 29 days (412 orbits) and a local equator overpass time of 09:30 LT (local time) on the descending node. The spatial resolution of the GOME-2 instrument on board the MetOp-A satellite (GOME-2A) is 40 km (across-track) $\times$ 40 km (alongtrack) while the spatial resolution the GOME-2 instrument on board the MetOp-B satellite (GOME-2B) is 80 km (across-track) $\times$ 40 km (alongtrack). A more detailed introduction to the MetOp series of satellites as well as the GOME-2 instrument on board can be found in Callies et al. (2000); Klaes et al. (2007); Munro et al. (2016).

The GOME-2 water vapour product is processed with GOME Data Processor (GDP) version 4.8 at the German Aerospace Center (DLR) within the framework of EUMETSAT's Satellite Application Facility on Atmospheric Composition Monitoring (AC-SAF). Slant columns water vapour are retrieved in the visible red wavelength range of 614 - 683 nm. The water vapour slant columns are then converted to vertical columns using air mass factors derived from the oxygen slant columns measured in the same wavelength band. The GOME-2 water vapour product has been validated intensively by radiosonde and Global Positioning System (GPS) measurements (Antón et al., 2015; Román et al., 2015; Kalakoski et al., 2016; Vaquero-Martínez et al., 2018). Detailed global comparison study shows that the GOME-2 TCWV has a dry bias of 3 % comparied to radiosonde data, while a wet bias of 3 - 5 % is observed compared to GPS observations (Kalakoski et al., 2016). Compared to ERA-Iterim reanalysis data, the GOME-2 water vapour product has been reported to significantly underestimate TCWV over central Africa by $\sim$10 kg m^{-2} and India by 15 - 21 kg m^{-2} (Grossi et al., 2015). A small wet bias of 4 - 8 kg m^{-2} is found over oceans in the tropics during summer of the northern hemisphere (Grossi et al., 2015). Compared to radiosonde measurements in the middle to high latitudes in the Northern Hemisphere, the GOME-2 product has in general a dry bias of 9 - 11 % (Antón et al., 2015). While a wet bias of 10 - 16 % is reported over Spain compared to GPS observations (Román et al., 2015; Vaquero-Martínez et al., 2018). The GOME-2 level 2 TCWV data is available on the AC-SAF webpage (`https://acsaf.org/`).

2.4. MODIS TCWV product

The MODerate resolution Imaging Spectroradiometer (MODIS) instruments are passive nadir viewing imaging sensors (Salomonson et al., 1989; King et al., 1992) on board the Earth Observing System's (EOS) Terra and Aqua satellites. The Terra satellite orbits on a sun-synchronous orbit with a local equator overpass time of 13:30 LT (local time) on descending node, while the local equator overpass time for the Aqua satellite is 10:30 LT on ascending node. MODIS measures earthshine radiance at 36 discrete wavelength bands from 0.4 μm up to 14.4 μm with various spatial resolutions, providing global observation every 1 - 2 days. Columnar water vapour content is derived from MODIS observations in the near infrared (NIR) from 865 - 1240 nm. The inversion of water vapour columns is based on the attenuation of radiation through the atmosphere. A more detailed description of the MODIS water vapour retrieval algorithm can be found in Kaufman and Gao (1992); Gao and Kaufman (2003). Due to the similar overpass time, water vapour product derived from the MODIS instruments on board the Terra satellite is used to validate the TROPOMI TCWV data set. Compared to GPS observations, the MODIS water vapour product in general shows a dry bias of 3 - 13 kg m^{-2} (Liu et al., 2006; Prasad and Singh, 2009). The NASA MOD05 monthly level 3 data product with a spatial resolution of $0.25° \times 0.25°$ is used in this study. The data is available to public at the NASA Earth Observations (NEO) webpage (`https://neo.gsfc.nasa.gov/`).

2.5. SSMIS TCWV product

Another data set used to validate the new TROPOMI water vapour retrieval is the atmospheric water vapour product derived from the Special Sensor Microwave Imager Sounder (SSMIS) on board the United States Air Force Defense Meteorological Satellite Program (DMSP) F16 polar orbiting satellite. The F16 satellite orbits at an altitude of $\sim$848 km on a sun-synchronous orbit with local equator crossing time of $\sim$16:00 LT on the ascending and $\sim$04:00 LT on the descending node. The SSMIS instrument on board the F16 satellite has been in operation since 2005, providing long term climate records of wind speed, cloud liquid water, atmospheric water vapour and rainfall rate during both day and night time (Wentz, 2015). SSMIS water vapour data are processed by Remote Sensing Systems with funding from the NASA MEaSUREs Program and the NASA Earth Science Physical Oceanography Program. The retrieval of water vapour columns is based on the radiative transfer calculation of brightness temperature over oceans. This type of satellite borne microwave observations of TCWV has been reported to show a wet bias of 2 - 3 $kg\,m^{-2}$ over ocean (Stephens et al., 1994). Although SSMIS shows smaller bias than GOME-2 and MODIS observations, it only provide measurements over ocean. More detailed introduction of the SSMIS TCWV retrieval algorithm can be found in Wentz (1997). In this study, the NASA SSMIS monthly level 3 product version 7 with spatial resolution of $0.25° \times 0.25°$ is used to validate the TROPOMI observations of TCWV. The data is available at the NASA Global Hydrometeorology Resource Center (GHRC) (`https://ghrc.nsstc.nasa.gov/`).

3. TROPOMI TCWV retrieval

The TROPOMI TCWV algorithm is developed based on the TCWV retrieval developed for GOME-2 at the blue spectral band (Chan et al., 2020) with improvements of spectral retrieval, air mass factor calculations, and a new algorithm to retrieve surface properties from TROPOMI observations. The retrieval follows the typical two steps retrieval approach for weak absorbers. The first step is the spectral analysis to retrieve water vapour slant columns from TROPOMI measurement spectra. The second step is the slant columns to vertical columns conversion using air mass factors. The following describes the water vapour column retrieval focusing on the differences to the GOME-2 TCWV algorithm.

3.1. Spectral retrieval of water vapour slant column

Slant column densities (SCDs) of water vapour are determined by applying the differential optical absorption (DOAS) technique (Platt and Stutz, 2008) to TROPOMI radiance spectra in the wavelength range of 435 - 455 nm with a daily measured solar irradiance spectrum as reference. Absorption cross sections of several species are used in the DOAS analysis for the retrieval of water vapour slant columns. These are water vapour at 296 K from the HITRAN database (Rothman et al., 2009), NO_2 at 220 K (Vandaele et al., 2002), O_3 at 228 K (Brion et al., 1998), O_4 at 293 K (Thalman and Volkamer, 2013) and liquid water at 297 K (Pope and Fry, 1997). A Ring spectrum is also included in the DOAS fit as pseudo cross section, to compensate for the Raman scattering effect. These cross sections are pre-convoluted to the TROPOMI spectral resolution for each detector row using the TROPOMI instrument spectral response functions (version 3.0.0) (Kleipool et al., 2018). Wavelength calibrations are performed by mapping the TROPOMI solar irradiance spectrum with a high resolution solar reference spectrum (Chance and Kurucz, 2010). The broad band spectral structures caused by broad band absorption of trace gases, instrumental effects, Rayleigh and Mie scattering are removed by including a 4^{th} order polynomial in the spectral fitting. Shift and stretch parameters of radiance spectra are also fitted during the spectral fitting process, to compensate for spectral instability due to small thermal variations within the spectrograph.

Table 1: Summary of the water vapour slant column retrieval results with different spectral fitting window for TROPOMI measurements taken on 1^{st} July 2018 (orbit 3698 - 3711) over the tropics (30°S - 30°N).

Fitting Window	Length of Fitting Window	Median SCD ($kg\,m^{-2}$)	Median Root Mean Square of Fit	Reference
430.0 - 450.0 nm	20.0 nm	40.01	6.94×10^{-4}	Wagner et al. (2013); Borger et al. (2020)
430.0 - 480.0 nm	50.0 nm	35.70	7.19×10^{-4}	Wang et al. (2014)
427.7 - 465.0 nm	37.3 nm	38.21	6.97×10^{-4}	Wang et al. (2016)
432.0 - 466.5 nm	34.5 nm	38.01	6.67×10^{-4}	Wang et al. (2019)
427.7 - 455.0 nm	27.3 nm	40.45	7.05×10^{-4}	Chan et al. (2020)
435.0 - 455.0 nm	20.0 nm	39.96	6.41×10^{-4}	This work

The spectral fitting window for the retrieval of water vapour slant columns is selected based on a sensitivity study with different spectral fitting windows. The DOAS fitting range used by several authors, and our water vapour slant column retrieval results are shown in Table 1. We vary the spectral fitting window with other retrieval settings unchanged. These spectral fitting windows for water vapour retrieval cover the featuring water vapour absorption structure at 441 - 448 nm. The median water vapour slant columns and the median root mean squares of spectral fit for measurements taken on 1^{st} July 2018 (orbit 3698 - 3711) over the tropics (30°S - 30°N) are shown in Table 1. The spectral fitting range at 435 - 455 nm leads to the lowest root mean square and the median SCD is also close to the median value amount all settings. Therefore, the fit window of 435 - 455 nm is chosen as the standard setting in this study.

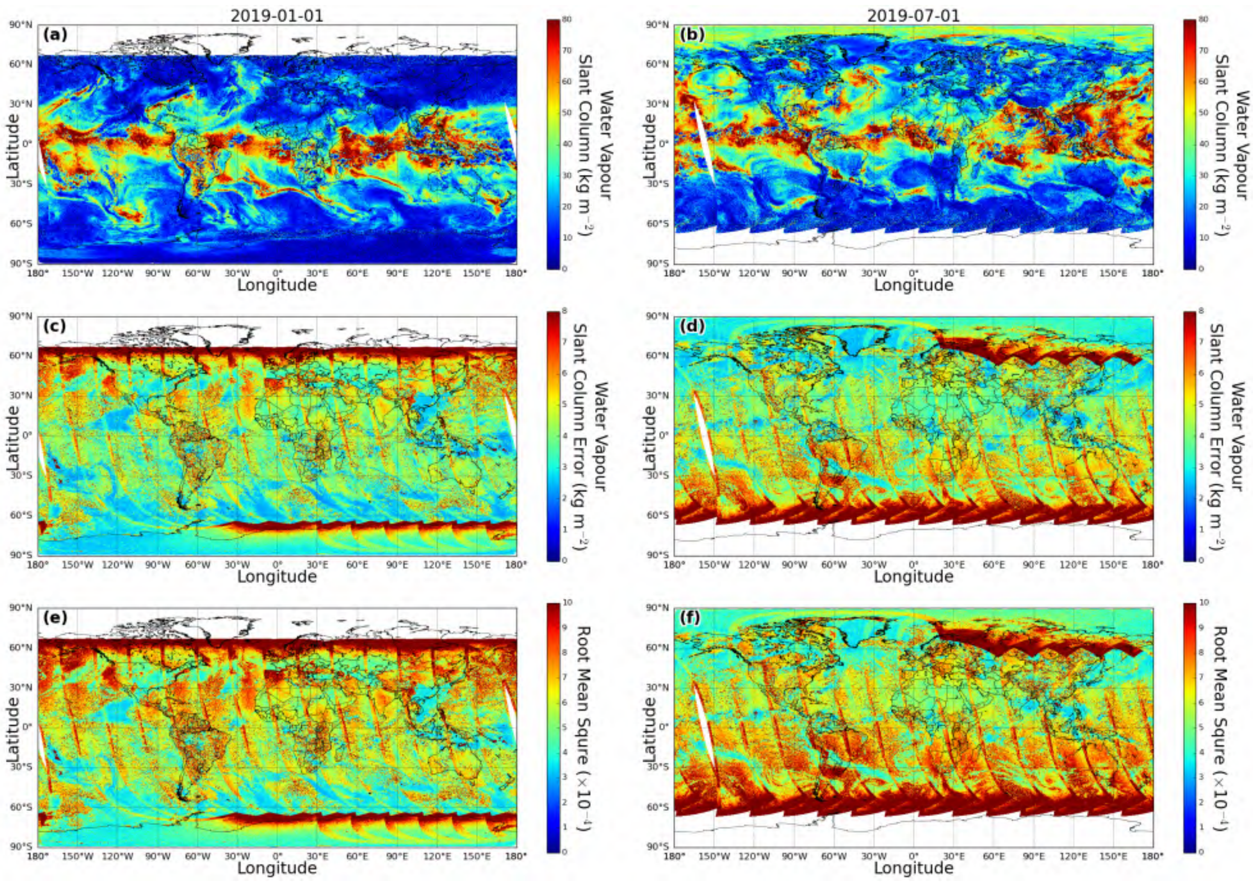

Figure 1: The top panels show water vapour slant columns retrieved from TROPOMI observations. The corresponding water vapour slant column uncertainties and the root mean square of the spectral fit residual are shown in the middle and bottom panels, respectively. TROPOMI data taken on 1^{st} January (the left column) and 1^{st} July 2019 (the right column) are shown.

Figure 1a & b show water vapour slant columns retrieved from TROPOMI observations on 1^{st} January and 1^{st} July 2019. The corresponding slant column uncertainties and the root mean square of the spectral fit residual are also shown. Higher water vapour slant columns can be observed over tropical regions, while upper latitudes in general show lower values. The measurement uncertainties and the root mean square of spectral fit residual are higher at both edges of the swath. This is related to the pixel binning scheme of the detector row of TROPOMI (Kleipool et al., 2018) which results in lower signal to noise levels at the edges. Higher uncertainties and root mean square are also found at both ends of the measurement orbit, where observations are taken with high solar zenith angles (thus, lower radiance intensity and signal to noise ratio).

3.2. Air mass factor

The retrieved water vapour SCDs are then converted to vertical column densities (VCDs or total columns) using air mass factors (AMFs) (Solomon et al., 1987; Palmer et al., 2001). As the DOAS retrieval of water vapour SCDs is applied to a relatively narrow spectral window of 20 nm, the wavelength dependency of optical path within this narrow spectral interval is negligible. The AMF can therefore be calculated at a representative wavelength. A prominent absorption line feature of water vapour is located at 442 nm. Therefore, the AMF is computed at this wavelength.

Assuming the atmosphere is optically thin, the height dependent measurement sensitivity can be decouple from the vertical distribution of optically thin absorbers (Palmer et al., 2001). The AMF can then be calculated using the box air mass factor (ΔAMF) at each height level following Equation 1.

$$AMF = \frac{SCD}{VCD} = \frac{\sum_{l=surface}^{l=TOA} \Delta AMF_l \times \Delta z_l \times c_l}{\sum_{l=surface}^{l=TOA} \Delta z_l \times c_l} \tag{1}$$

where Δz_l is the thickness of layer l and c_l is the number density of the absorber. Information of c_l is typically taken from the a priori profile.

3.2.1. Box air mass factor look-up table

Due to the complexity of the optical path in the atmosphere, the calculations of the height-dependent measurement sensitivity (or ΔAMF) typically rely on comprehensive radiative transfer calculations. The ΔAMFs are independent of the vertical distribution of the absorber, but strongly dependent on surface reflectivity, surface height, solar and viewing geometries. In this study, ΔAMFs are calculated using the radiative transfer model VLIDORT version 2.7 (Spurr, 2008) at 442 nm with an aerosol free US standard atmosphere (Anderson et al., 1986). The ΔAMFs are pre-calculated with a number of representative viewing zenith angle (α), solar zenith angle (θ), relative azimuth angle (ϕ), surface albedo (A_s) and surface pressure (P_s) and stored in a look-up table in order to reduce the processing time. The ΔAMFs for each TROPOMI observation are derived by interpolation within the look-up table. The parameterizations of the ΔAMF look-up table are similar to the one used in GOME-2 TCWV retrieval (Chan et al., 2020).

3.2.2. *Water vapour vertical profile*

The calculation of AMF is also dependent on the vertical distribution profile of water vapour (see Equation 1). A dynamic search approach is used to find the optimal a priori water vapour profile for AMF calculation. This approach has been implemented and validated for the retrieval of TCWV from GOME-2 observations in the blue band (Chan et al., 2020). The dynamic search approach is based on the fact that the vertical distribution of water vapour is strongly dependent on its total column. A water vapour vertical profile look-up table is created based on statistical analysis of historical water vapour profiles. The look-up table contains geolocation dependent water vapour vertical profiles and their variation ranges for each month of the year. This look-up table is then used as auxiliary input for the optimization of the water vapour profile.

An iterative approach is employed to optimize the a priori water vapour used in the retrieval. The iteration begins with the mean profile of the satellite measurement location of the corresponding month. This mean profile is then used together with the corresponding ΔAMFs to calculate an initial AMF following Equation 1. The retrieved water vapour SCD is divided by this initial AMF to retrieve the initial VCD. The water vapour profile look-up table is then linearly interpolated to the resulting initial column to retrieve the corresponding water vapour profile. The new profile is again used to retrieve the second VCD. This process repeats until the difference between the input and output VCD is less than 1 % or the number of iteration reaches the limit. The maximum number of iteration allowed in the current version of retrieval is set to 5. This limit is considered realistic as the retrieval of more than 99 % of TROPOMI measurements stopped within 3 iterations.

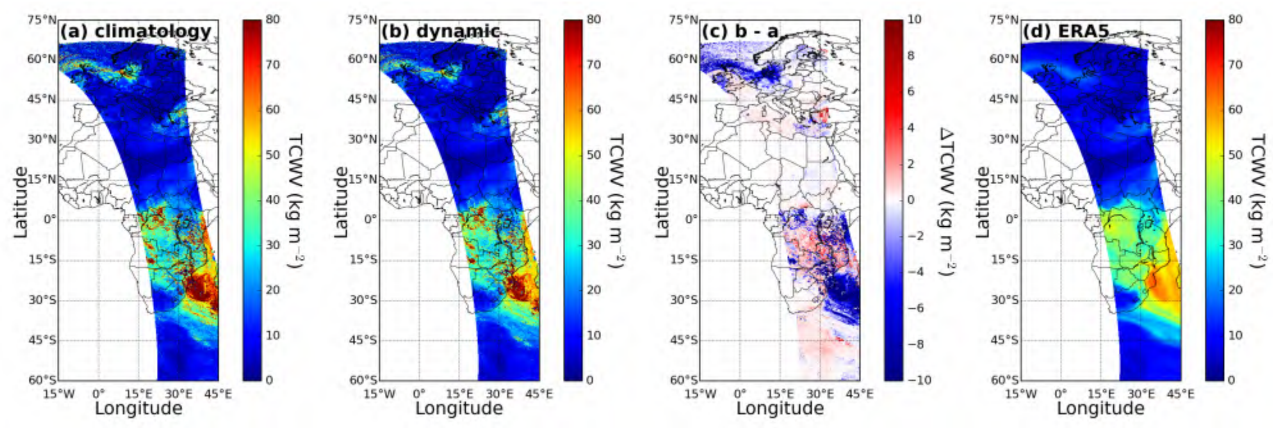

Figure 2: Comparison of TCWV retrieved with (a) climatology and (b) dynamic a priori water vapour profile. The differences between (a) and (b) are indicated in (c). ERA5 reanalysis data interpolated to TROPOMI overpass time is also shown in (d) for reference. TROPOMI data measured on 15^{th} January 2019 (orbit 6513) over Africa and Europe is shown. No cloud filtering is applied to the data shown in the figure.

A comparison of TCWV retrieved with climatology (a) and with a dynamic a priori water vapour profile (b) is shown in Figure 2, for the 15^{th} of January 2019 over Africa and Europe. No cloud filtering is applied to the data shown in Figure 2. The differences between the two retrievals is shown in Figure 2c. For reference, ERA5 reanalysis data interpolated to TROPOMI overpass time is shown in Figure 2d. Compared to the climatology a priori approach, the dynamic a priori approach reduces the retrieved TCWV over areas with high TCWV. This is mainly due to the fact that water vapour is concentrated in the lower troposphere when TCWV is relatively small (i.e., $<30\,\mathrm{kg\,m^{-2}}$), while higher TCWV usually is associated with enhanced water vapour concentration in the upper altitudes (Chan et al., 2020). Therefore, the change in vertical profile shape would result in larger AMFs when TCWV is high and yield lower TCWV.

3.2.3. Surface albedo

Surface albedo is an important parameter for the calculation of the air mass factor. The sensitivity of satellite observations, especially to the lower troposphere where most water vapour resides, is strongly related to surface albedo. The surface albedo used in this study is retrieved from TROPOMI observations using the full-physics inverse learning machine (FP_ILM) algorithm (Loyola et al., 2020). The FP-ILM algorithm is a machine learning based approach that aims to derive the relationship (inverse function) between the parameter of interest (surface albedo in this case) and measured radiance spectrum (with other atmospheric parameters). This algorithm has been applied to O_3 profile shape and SO_2 plume height retrievals (Efremenko et al., 2017; Xu et al., 2017; Hedelt et al., 2019). Training of the FP_ILM algorithm is driven by a set of synthetic data generated with a radiative transfer model. Synthetic TROPOMI radiance spectra at 435 - 455 nm are simulated using the radiative transfer model VLIDORT version 2.7 (Spurr, 2008) together with the smart sampling technique (Loyola et al., 2016). For the training, the inputs are DOAS fitted parameters, as well as the solar/satellite viewing geometry and surface pressure. The inversion result is the Geometry-dependent effective Lambertian equivalent reflectivity (GE_LER) and it is retrieved for clear sky observations (cloud fraction <0.05). Compared to the Lambertian equivalent reflectivity (LER) climatology derived from Ozone Monitoring Instrument (OMI) observations (Kleipool et al., 2008), which is being used in most of the operational TROPOMI products. As the OMI albedo product is derived from observations in 2004 - 2007, TROPOMI albedo derived in 2018 - 2021 is expected to better capture the actual surface conditions, especially with regard to temporal variability.

Surface GE_LER derived from TROPOMI observations in the spectral band of 435 - 455 nm is compared to the OMI monthly minimum LER climatology derived at 442 nm (Kleipool et al., 2008). Figure 3 shows the TROPOMI GE_LER and OMI monthly minimum climatology for January and July. Differences between the two data sets are also shown. Surface GE_LER derived from TROPOMI is on average ∼0.04 lower than OMI climatology. Our result is consistent with a previous study, that found slightly lower GE_LER retrieved from TROPOMI with the FP_ILM algorithm compared to the OMI climatology in a similar wavelength band (Liu et al., 2021). The TROPOMI GE_LER in general shows ∼0.05 lower albedo over sub-tropics compared to OMI climatology. Relatively larger discrepancies (>0.2) can be observed over areas covered with snow or ice. Previous study reported that OMI typically overestimated albedo in high latitudes and the Arctic by 0 – 11 % compared to ground based measurements (Bernhard et al., 2015). In addition, the OMI climatology is derived from measurements taken in 2004 - 2007, the TROPOMI GE_LER derived in the same measurement period of 2018 - 2021 is expected to better capture the actual conditions. Higher albedo is observed over desert, e.g., the Sahara, Arabian and Gobi desert. This is likely related to aerosol effects, as aerosol is not modelled explicitly in the generation of synthetic spectra used for the training of the inverse model. Other effects, like difference in wavelength and measurement period, might also contribute to the difference in albedo. Further investigation

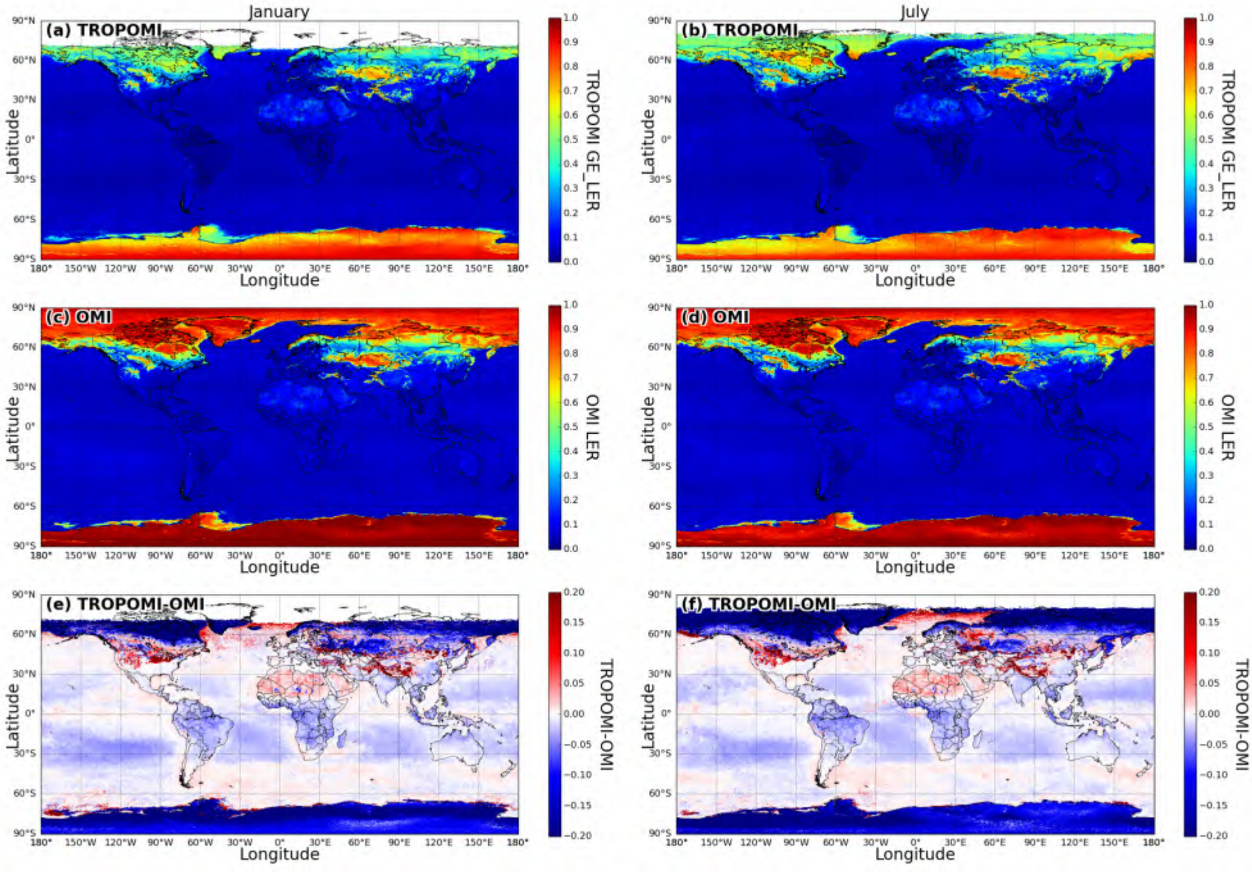

Figure 3: Surface GE_LER derived from TROPOMI observations (top panels) and OMI monthly minimum LER (middle panels) for January (left column) and July (right column). The bottom panels show the differences between the two dataset. TROPOMI LER data is derived in the spectral band of 435 - 455 nm, while OMI LER data is retrieved at 442 nm.

is needed in order to quantify the impacts of aerosol on surface albedo retieval. We are planning to improve the surface albedo retrieval in the future by including aerosol filtering, using aerosol index data derived from TROPOMI.

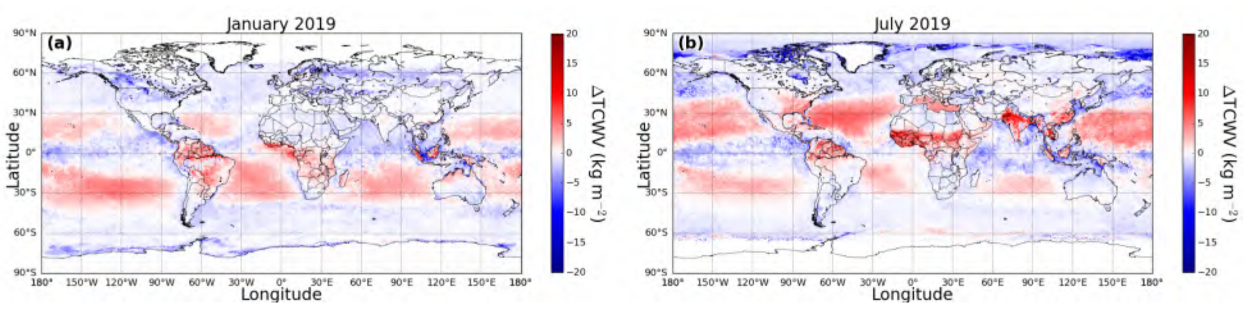

Figure 4: Differences of TROPOMI monthly averaged TCWV retrieved with TROPOMI GE_LER and OMI climatology in (a) January and (b) July 2019. Measurements with cloud radiance fraction below 0.5 are used for the calculation of monthly average.

As the OMI albedo climatology is being used in various operational TROPOMI products, e.g., Theys et al. (2017); De Smedt et al. (2018), we use this albedo product as reference for the investigation of the influence of albedo on TCWV retrieval. Compared to MODIS observations, the OMI climatology is on average 0.02 higher (Kleipool et al., 2008). Larger overestimation up to 0.06 is observed in the tropics over the Amazon, central Africa, India and Indonesia (Kleipool et al., 2008). Ground based observation comparison study shows that OMI albedo overestimated by $0-11\,\%$ over high latitudes and the Arctic. Figure 4 shows the differences of monthly averaged TROPOMI TCWV retrieved with TROPOMI GE_LER and OMI climatology for January and July 2019. Higher TCWV can be observed over ocean in the sub-tropics, which agrees with the differences between the two albedo data sets (see Figure 3e & f). Reduced albedo decreases the measurement sensitivity in the lower troposphere, and results in lower AMFs. This leads to increased TCWV. Larger discrepancies are also found over tropic and subtropic areas, e.g., the Amazon, central Africa, India and Indonesia. These discrepancies are mainly related to the bidirectional reflectance distribution function (BRDF) effect over vegetation and aerosol/cloud contamination. The TROPOMI GE_LER albedo data significantly improved the overestimation of albedo (and underestimation of TCWV) over these regions.

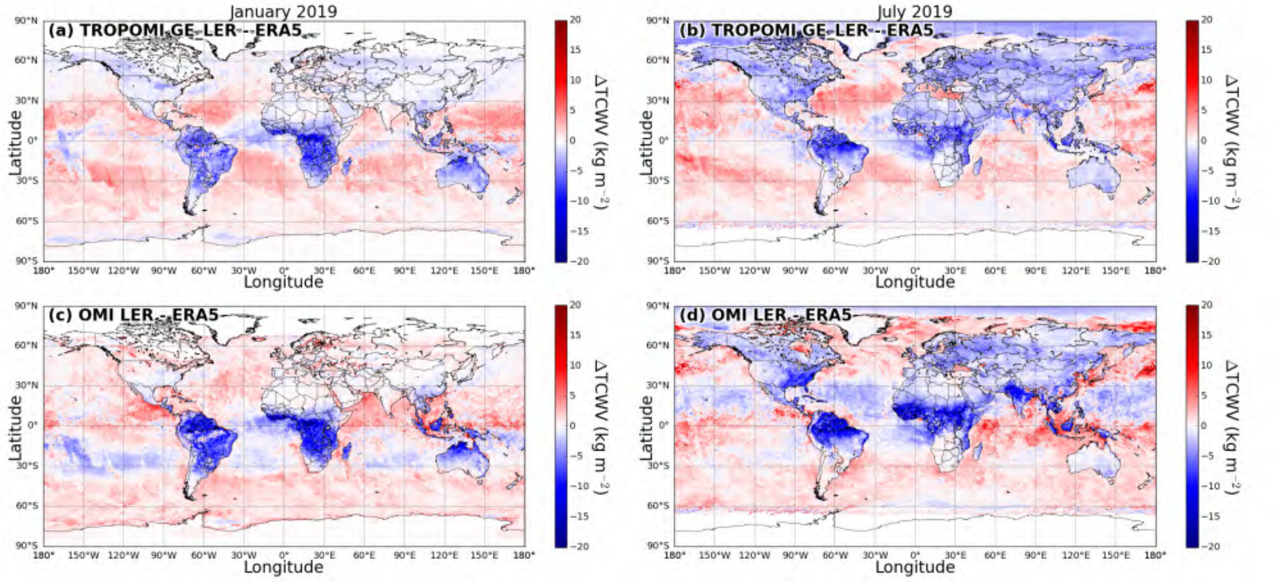

Figure 5: The top panels show the differences of monthly averaged TCWV retrieved with TROPOMI GE_LER and ERA5 reanalysis data, while the differences of monthly averaged TCWV retrieved with OMI LER and ERA5 reanalysis data are shown in the bottom panels. Data of January (the left column) and July 2019 (the right column) are shown. Measurements with cloud radiance fraction below 0.5 are used for the calculation of monthly average.

Table 2: Summary of the improvement related to the use of TROPOMI GE_LER over various areas.

Region	OMI LER		GE_LER	
	Absolute Bias ($\mathrm{kg\,m^{-2}}$)	Relative Bias (%)	Absolute Bias ($\mathrm{kg\,m^{-2}}$)	Relative Bias (%)
Amazon	-7.6 to -8.0	-16.2 to -17.7	-4.5 to -5.3	-9.7 to -11.8
Central Africa	-2.7 to -9.4	-6.5 to -24.7	-2.7 to -7.5	-6.5 to -20.0
India	-0.2 to -8.0	-1.7 to -15.3	-0.2 to -3.4	-1.8 to -6.4

Figure 5a & b show the comparisons of monthly averaged TCWV retrieved with TROPOMI GE_LER to ERA5 reanalysis data, while the comparisons of TCWV retrieved with OMI albedo to ERA5 reanalysis are shown in Figure 5c & d. Data from January and July 2019 are shown. Compared to ERA5, TCWV retrieved with OMI albedo shows larger underestimation over tropic and subtropic areas, e.g., the Amazon, central Africa, India and Indonesia. Higher OMI albedo over these areas enhanced the sensitivity in the lower troposphere which leads to larger AMFs and hence lower total columns. Although the retrieval with TROPOMI GE_LER has also lower TCWV over these regions, this underestimation is significantly improved. Table 2 summarized the improvement related to the use of TROPOMI GE_LER over various areas. Larger TCWV overestimation can be observed along the equator over ocean with retrievals using the OMI albedo. Compared to ERA5 data, the mean absolute bias of TROPOMI TCWV using OMI LER albedo in retrieval is 1.5 - 2.1 kg m^{-2}, while using TROPOMI GE_LER reduces the absolute mean bias to 1.3 - 2.1 kg m^{-2}.

3.2.4. Cloudy and partially cloudy measurements

Clouds are treated as opaque Lambertian surfaces in the TCWV retrieval. The treatment of partially cloudy pixels is based on the independent pixel approximation (Martin et al., 2002; Boersma et al., 2004) where the pixel is separated into two independent parts: one fully covered by clouds and the other completely cloud free. Air mass factors are calculated independently for both clear sky and cloudy parts. Cloud information, including cloud fraction (CF), cloud albedo (A_c) and cloud top pressure (P_c) are taken from the TROPOMI operational cloud product (Loyola et al., 2018).

The AMF for the cloudy part is calculated from the ΔAMF look-up table by setting the surface pressure (P_s) to cloud top pressure (P_c) and replacing the surface albedo (A_s) with the cloud albedo (A_c). The calculation of the slant column for the cloudy scene is insensitive to water vapour below the cloud, hence ΔAMFs below cloud are 0. On the other hand, the vertical column is calculated by integrating the water vapour profile from the surface to the top of atmosphere which includes the part below cloud (see Equation 1). The 'invisible' column below the cloud (also known as the 'ghost column') is taken from the a priori profile.

The AMF of a partially cloudy pixel is the intensity-weighted average of the cloudy AMF (AMF_{cld}) and clear sky AMF (AMF_{clr}). This weighting is commonly know as effective cloud fraction (CF_{eff}, or radiance cloud fraction) which is defined by Equation 2.

$$CF_{eff} = \frac{CF \times I_{cld}}{CF \times I_{cld} + (1 - CF) \times I_{clr}} \tag{2}$$

where I_{cld} and I_{clr} represent the radiance intensity for cloudy and clear sky scenes, respectively. The radiance intensities are pre-calculated using the radiative transfer model VLIDORT at 442 nm for a number of representative observation and solar geometries, surface (cloud) albedo and surface (cloud-top) pressure and stored in a look-up table. The settings of the intensity look-up table are the same as the ΔAMF look-up table without the pressure level dimension. The AMF can then be calculated following Equation 3.

$$AMF = AMF_{cld} \times CF_{eff} + AMF_{clr} \times (1 - CF_{eff}) \tag{3}$$

The resulting AMFs are used to divide the retrieved water vapour slant columns to convert to vertical columns.

3.3. Error estimation

The estimation of the uncertainty on retrieved TCWV from TROPOMI follows the one used for GOME-2 (Chan et al., 2020). It is separated into two major parts, slant column and air mass factor uncertainties. The uncertainty of TCWV can be expressed as Equation 4:

$$\sigma_{vcd}^2 = VCD^2 \times \left(\left(\frac{\sigma_{scd}}{SCD} \right)^2 + \left(\frac{\sigma_{amf}}{AMF} \right)^2 \right) \tag{4}$$

where σ_{vcd}, σ_{scd} and σ_{amf} are the uncertainty of TCWV, the uncertainty of water vapour slant column and air mass factor uncertainty, respectively. Details of the estimation of the water vapour slant column uncertainty and air mass factor error are as follows.

The uncertainties of water vapour slant column can be separated into two parts, random and systematic errors. Random error contributions are mainly from instrument noise, instrument characteristics and the uncertainties related to the DOAS retrieval of slant columns. Systematic errors are related to uncertainties on the instrument slit function, incomplete removal of stray light, wavelength calibration uncertainties, and uncertainties on absorption cross sections. The random part can be quantified by analyzing the spectral fit residual (Stutz and Platt, 1996). The systematic part is estimated through sensitivity tests using absorption cross sections at different effective temperatures, and using sightly different slit functions. We estimate that the systematic part is about 3 % (Chan et al., 2020). The uncertainty of the slant column may be calculated following Equation 5:

$$\sigma_{scd}^2 = \sigma_{scd_r}^2 + (0.03 \times SCD)^2 \tag{5}$$

where σ_{scd_r} is the random error estimated by analyzing the DOAS fit residual.

The uncertainty on AMF is mainly attributed to the uncertainty of the input parameters used in the AMF calculation. The AMF uncertainty related to each input parameter can be derived from the box air mass factor look-up table using the the finite difference method.

The uncertainty of surface albedo is assumed to relate to the albedo wavelength dependency. The albedo used in TROPOMI TCWV retrieval is derived at the spectral band of 435 - 455 nm, without spectral dependency. We took the OMI albedo product (Kleipool et al., 2008) as reference, and assume the albedo uncertainty equal to the difference between albedo derived at 425 nm and 452 nm. Uncertainties on water vapour profiles are estimated through the analysis of historical profiles, and their standard deviation of the variation are stored in a look-up table. The corresponding impact on the AMF calculation is estimated by adding 1 σ standard deviation to the water vapour profile for the AMF calculation. The difference between this AMF and the original AMF is then used as uncertainty. Surface pressure (or surface height) is taken from a digital elevation model (DEM) and the accuracy of DEM is usually in the range of 10 - 15 m (Mukherjee et al., 2013). Therefore, a relatively small uncertainty of 10 hPa is assumed. The uncertainty on the AMF for a clear sky scene can then be calculated following Equation 6:

$$\sigma_{amf}^2 = \left(\frac{\partial AMF}{\partial A_s} \sigma_{A_s} \right)^2 + \left(\frac{\partial AMF}{\partial P_s} \sigma_{P_s} \right)^2 + \left(\frac{\partial AMF}{\partial c_l} \sigma_{c_l} \right)^2 \tag{6}$$

where σ_{amf}, σ_{A_s}, σ_{P_s} and σ_{c_l} are the AMF uncertainty, surface albedo, surface pressure and water vapour profile, respectively.

For (partially) cloudy measurements, the uncertainty of cloud albedo is assumed to be 0.02 (Loyola et al., 2018), while uncertainty of cloud pressure is estimated to be 50 hPa (Theys et al., 2017; De Smedt et al., 2018). The uncertainty on the cloudy AMF can then be calculated as in Equation 6 by replacing surface albedo/pressure parameters by the corresponding cloud parameters.

The uncertainty of cloud fraction is ranging from 0.007 to 0.032 (Loyola et al., 2018). Therefore, we assume an effective cloud fraction uncertainty of 0.02 in the calculation of AMF uncertanity. The combined AMF uncertainty may then be expressed as Equation 7:

$$\begin{aligned}\sigma_{amf}^2 \quad = \quad & (AMF_{cld} \times CF_{eff})^2 \times \left(\left(\frac{\sigma_{amf_{cld}}}{AMF_{cld}} \right)^2 + \left(\frac{\sigma_{cf_{eff}}}{CF_{eff}} \right)^2 \right) \\ & + (AMF_{clr} \times (1 - CF_{eff}))^2 \times \left(\left(\frac{\sigma_{amf_{clr}}}{AMF_{clr}} \right)^2 + \left(\frac{\sigma_{cf_{eff}}}{1 - CF_{eff}} \right)^2 \right)\end{aligned} \tag{7}$$

where $\sigma_{cf_{eff}}$ is the uncertainty of effective cloud fraction, $\sigma_{amf_{clr}}$ represents the clear sky AMF uncertainty, and $\sigma_{amf_{cld}}$ denotes the cloudy AMF uncertainty. The final uncertainty on TCWV is then calculated following Equation 4.

Table 3: Summary of median estimated measurement error at different latitudes and sky conditions.

Latitude	Estimated Error		
	All Sky	Clear Sky (CF_{eff}<0.5)	Cloudy Sky (CF_{eff}>0.5)
Tropics (0° - 30°)	5.0 $kg\,m^{-2}$ (18.2 %)	4.4 $kg\,m^{-2}$ (14.0 %)	8.8 $kg\,m^{-2}$ (27.4 %)
Midlatitudes (30° - 60°)	4.1 $kg\,m^{-2}$ (33.9 %)	4.0 $kg\,m^{-2}$ (32.7 %)	4.3 $kg\,m^{-2}$ (34.5 %)
Polar (60° - 90°)	1.3 $kg\,m^{-2}$ (38.8 %)	1.0 $kg\,m^{-2}$ (43.4 %)	3.1 $kg\,m^{-2}$ (34.9 %)

The estimated uncertainties of TCWV for TROPOMI observations at different latitudes and sky conditions are summarized in Table 3. The estimated error is in general lower for measurement taken under clear sky conditions (effective cloud fraction <0.5) compared to cloudy conditions (effective cloud fraction >0.5). However, the relative error for clear and cloudy sky measurements are quite similar at midlatitudes and polar regions. Cloudy measurements are usually associated with higher TCWV, and hence leads to lower relative error.

3.4. Gridding and averaging

Pixels from different orbits often overlap in higher latitudes. In order to compare to other data sets, the retrieved TCWV is binned to a regular latitude-longitude grid. We use a grid with a spatial resolution of $0.25° \times 0.25°$. The gridding process considers the overlapping area of the TROPOMI ground pixel and the latitude-longitude grid. The percentage of overlap is calculated and used as weight for the calculation of the mean grid cell value. The gridded TCWV can be express as Eq. 8:

$$VCD_g = \frac{\sum_{i=1}^{n} VCD_i \times w_i}{\sum_{i=1}^{n} w_i} \tag{8}$$

where VCD_g is the gridded TCWV while VCD_i represents each individual measurement that touches the grid cell. The weights are denoted as w which is the percentage of the grid cell covered by the satellite pixel.

The gridded TCWV is based on all valid vertical columns within a certain period, for example a day or a month. The root mean square of spectral fit residual is a good indicator of the measurement signal to noise ratio, and solar zenith angle is strongly related to the radiance intensity, therefore, they are used as data filtering criteria. Clouds shield water vapour in the lower troposphere and affect the measurement quality. In addition, small AMF indicated that most of the information is coming from the a priori profile instead of the measurement. Therefore, it is necessary to filter data with significant cloud contamination and low AMF. In the gridding process, we only use data with solar zenith angle smaller than 85°, effective cloud fraction (or radiance cloud fraction) smaller than 0.5, root mean square of spectral fit residual less than 0.002, and AMF larger than 0.1.

4. Validation

In this section, we present the validation results of the retrieved TROPOMI TCWV data set. TROPOMI TCWV is compared to ERA5 reanalysis data, GOME-2, MODIS and SSMIS satellite observations. Brief descriptions of these data sets can be found in Section 2. Validation against ground based observations will be addressed in separate studies.

4.1. Spatial distribution comparison

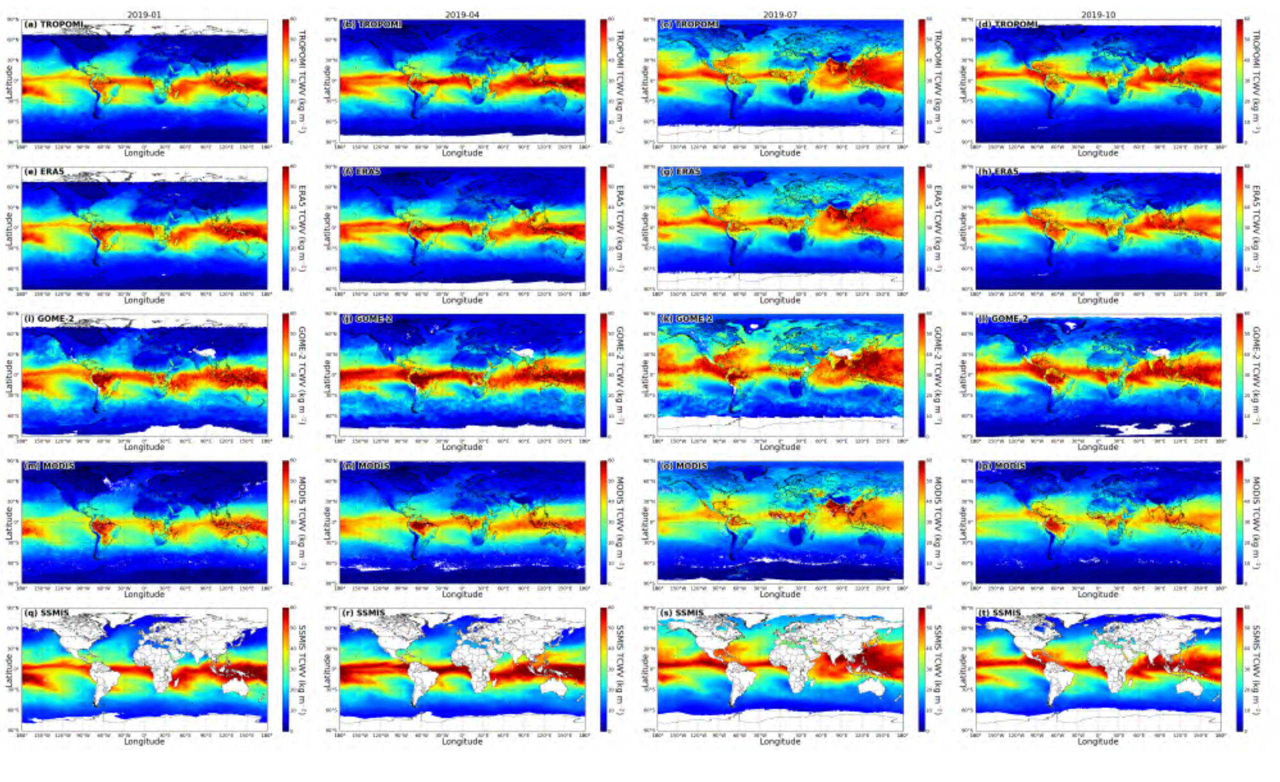

Figure 6: Monthly averaged TCWV from TROPOMI (1^{st} row), ERA5 reanalysis data (2^{nd} row), GOME-2A & B (3^{th} row), MODIS Terra (4^{th} row), and SSMIS (5^{th} row). Data from January (1^{st} column), April (2^{nd} column), July (3^{th} column) and October (4^{th} column) of 2019 are shown. Note that SSMIS only provide data over surface covered by water.

Figure 6 shows the monthly average spatial distribution of TCWV from TROPOMI, ERA5, GOME-2, MODIS, and SSMIS for January, April, July and October of 2019. These months are chosen as examples for winter, spring, summer and autumn, respectively. All data sets are in spatial resolution of $0.25° \times 0.25°$. Missing data are mainly due to the filtering of measurements with solar zenith angle larger than 85°. All five data sets show similar spatial patterns of water vapour. TROPOMI observations in general agree well with ERA5 reanalysis, while underestimation of TCWV can be observed over tropic and subtropic areas, e.g., the Amazon, central Africa, India and Indonesia. These discrepancies are probably related to albedo effects in the visible band over vegetation and aerosol/cloud contamination. Compared to GOME-2 and SSMIS observations, TROPOMI data in general shows lower values over ocean in the tropics, especially along the equator. This discrepancy is partly related to the differences in satellite overpass time and measurement wavelength band. We have assessed the effect of different satellite overpass time on TCWV values by comparing ERA5 data during GOME-2 (∼09:30 LT) and TROPOMI (∼13:30 LT) overpass time. The results shows that ERA5 TCWV is in the morning (∼09:30 LT) in general 4 - 6 % higher than that at noon (∼13:30 LT). In addition, microwave measurements (i.e., SSMIS) are sensitive to water vapour within and below clouds (except some very thick rain clouds) and provide observations of TCWV in all sky conditions over ocean, while measurements in the visible band (i.e., TROPOMI) are strongly influenced by clouds. Proper cloud screening has to be applied to remove cloud contaminated data. As TCWV under cloudy conditions is expected to be higher, filtering cloudy data would result in a dry bias in the average values. Compared to MODIS observations, TROPOMI measurements in general show higher TCWV over oceans. MODIS NIR measurements are known to be less sensitive to water vapour in the lower troposphere over oceans due to low albedo at this wavelength band. Previous studies reported that MODIS is underestimating TCWV by 3 - 13 kg m^{-2} (Liu et al., 2006; Prasad and Singh, 2009), and our result is consistent with these studies.

4.2. Correlation and bias

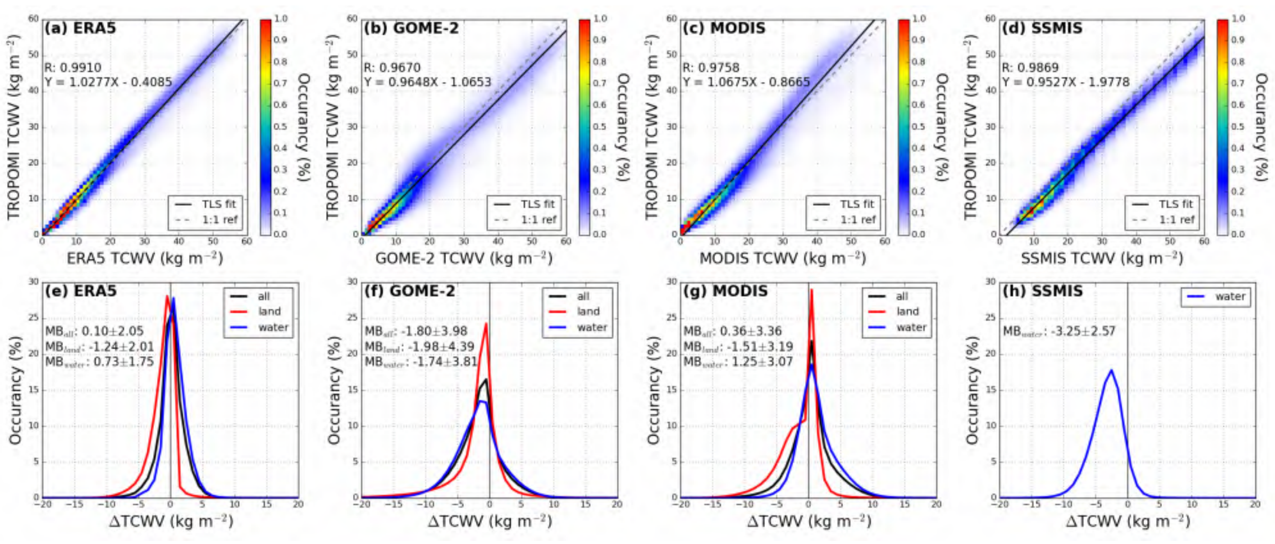

Figure 7: Comparison of TROPOMI TCWV to (a) ERA5 reanalysis data, (b) GOME-2, (c) MODIS, and (d) SSMIS observations. Histograms of the differences of TCWV between TROPOMI and reference data sets are shown in the bottom panels. Monthly averaged data from May 2018 to May 2021 with spatial resolution of $0.25° \times 0.25°$ are used in the comparison.

The statistical comparisons of TROPOMI TCWV to ERA5 reanalysis data, GOME-2, MODIS, and SSMIS observations are shown in Figure 7a-d, respectively. Histograms of the differences of TCWV between TROPOMI observations and reference data sets are shown in Figure 7e-h. The histograms of measurements over land (red lines), water (blue lines) and all surface (black lines) are shown. Monthly averaged data from May 2018 to May 2021 with spatial resolution of $0.25° \times 0.25°$ are used in the comparison. The scatter plots show that TROPOMI observations agree well with the reference data sets, with a Pearson correlation coefficient (R) range from 0.96 to 0.99. The discrepancies over different surfaces are shown in the Histograms. Compared to ERA5, TROPOMI observations on average underestimate TCWV by $1.24\,\mathrm{kg\,m^{-2}}$ over land, while a small wet bias of $0.73\,\mathrm{kg\,m^{-2}}$ is observed over water. Compared to GOME-2 measurements, TROPOMI data shows a dry bias of $1.74\,\mathrm{kg\,m^{-2}}$ and $1.98\,\mathrm{kg\,m^{-2}}$ over land and water, respectively. Part of the discrepancy between TROPOMI and GOME-2 is related to the difference in overpass time (see Section 4.1), which account for approximately $1\,\mathrm{kg\,m^{-2}}$ of the dry bias. The comparison to MODIS data shows a wet bias of $1.25\,\mathrm{kg\,m^{-2}}$ over water and a dry bias of $1.51\,\mathrm{kg\,m^{-2}}$ over land. TROPOMI observations over water are on average $3.25\,\mathrm{kg\,m^{-2}}$ lower than SSMIS data. Details of the correlation and bias compared to the reference data sets are summarized in Table 4. Our result is in line with the previous study that SSMIS data in general shows a wet bias of $2\text{-}3\,\mathrm{kg\,m^{-2}}$ (Stephens et al., 1994).

Table 4: Summary of correlation and bias for the comparison of TROPOMI TCWV against different data sets.

Data set	Land		Water		All Surface	
	R	Bias ($\mathrm{kg\,m^{-2}}$)	R	Bias ($\mathrm{kg\,m^{-2}}$)	R	Bias ($\mathrm{kg\,m^{-2}}$)
ERA5	0.990	-1.24 $\pm$ 2.01	0.994	0.73 $\pm$ 1.75	0.991	0.10 $\pm$ 2.05
GOME-2	0.952	-1.98 $\pm$ 4.39	0.970	-1.74 $\pm$ 3.81	0.967	-1.80 $\pm$ 3.98
MODIS	0.979	-1.51 $\pm$ 3.19	0.984	1.25 $\pm$ 3.07	0.976	0.36 $\pm$ 3.36
SSMIS	–	–	0.987	-3.25 $\pm$ 2.57	–	–

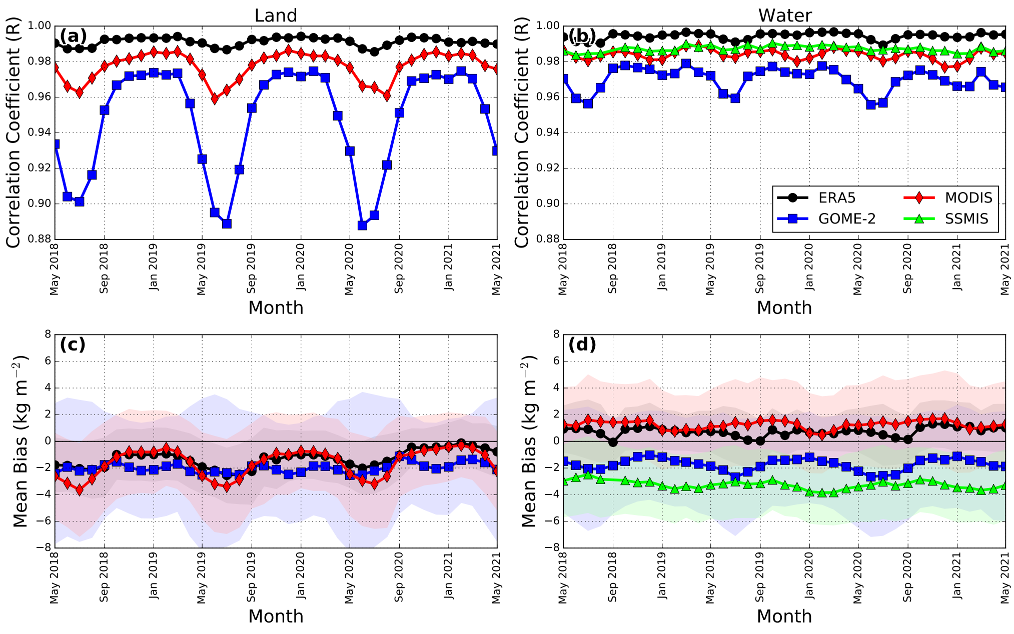

Figure 8: Time series of correlation coefficient (upper panels) and bias (bottom panels) between TROPOMI and reference data sets. Comparison over land (left panels) and water (right panels) are shown. Comparison to ERA5 (black lines), GOME-2 (blue lines), MODIS (red line), and SSMIS (green line) are indicated. Shadowed areas indicate $1\,\sigma$ variation range.

Figure 8 shows the time series of correlation coefficient and bias of TCWV between TROPOMI and reference data sets. Statistical parameters for observations over land and water from May 2018 to May 2021 are shown. The correlation between the TROPOMI observations and reference data sets is in general very good, with a Pearson correlation coefficient (R) ranging from 0.89 to 0.99 over land, and 0.95 to 0.99 over water. TROPOMI data agrees better with ERA5 reanalysis data with R of 0.98 - 0.99, while a lower correlation coefficient R of 0.88 - 0.98 is found in the comparison to GOME-2 observations. The correlation between TROPOMI and reference data sets shows a seasonal pattern, with higher correlation during winter of the Northern Hemisphere and lower during summer. This effect is more significant for observations over land, especially in the comparison with GOME-2 observations. We attribute the relatively larger seasonal effect for the comparison to GOME-2 to the differences in overpass time (TROPOMI at ∼13:30 LT, GOME-2 at ∼09:30 LT) and seasonal variations of the diurnal pattern of water vapour. The remaining discrepancies are mainly due to the sensitivity of different wavelength bands in relation to the seasonal variation of surface albedo and cloud/aerosol conditions. This effect has been reported in the comparison of GOME-2 observations in the blue and red band (Chan et al., 2020). TROPOMI observations in general underestimate TCWV over land by 0.3 - 3.6 $\mathrm{kg\,m^{-2}}$. The comparison of TROPOMI TCWV to ERA5 and MODIS over water shows a wet bias from 0 - 1.7 $\mathrm{kg\,m^{-2}}$, while the comparison to GOME-2 and SSMIS shows a dry bias from 1.1 - 3.8 $\mathrm{kg\,m^{-2}}$. The dry bias is more significant in summer of the Northern Hemisphere. Considering the differences in measurement time and measurement sensitivity, the small discrepancies among these data sets are considered reasonable.

4.3. Zonal comparison

Water vapour columns derived from TROPOMI and reference data sets are sorted by their latitudes with 1° resolution for each month; the resulting time series are shown in Figure 9. Observations over land and water are separated in the comparison. Monthly averaged data from May 2018 to May 2021 are shown. The zonal mean values at different latitude bands are summarized in Table 5. TROPOMI retrieval of TCWV in general shows good zonal agreement with other data sets, indicating all data sets captured similar spatio-temporal variations of water vapour. Higher values are observed over tropical regions over both land and water, while TCWV at upper latitudes is in general much lower. Significant seasonal patterns are also observed in all data sets, with higher columns during summer and lower values in winter (of the corresponding hemisphere). Compared to ERA5 data, the dry bias of TROPOMI over lands in the tropics (15° S - 15° N) is slightly higher (1 - 2 $\mathrm{kg\,m^{-2}}$) than that at upper latitudes, while a small wet bias of 1 - 3 $\mathrm{kg\,m^{-2}}$ are observed over water in the subtropics (15° - 30°). The wet bias over water along equator is almost 0.

For the comparison to GOME-2 observations, a clear north-south dependency is observed. Dry bias of TROPOMI over lands in the tropic and subtropic areas in the Southern Hemisphere (0 - 30 ° S) are significantly higher (∼5 $\mathrm{kg\,m^{-2}}$) than that in the Northern Hemisphere. TROPOMI also measured higher TCWV than GOME-2 (1 - 4 $\mathrm{kg\,m^{-2}}$) over water in tropic and subtropic areas in the Southern Hemisphere (0 - 30 ° S), while this bias is much less pronounced in the Northern Hemisphere. The north-south dependency of discrepancy between GOME-2 and TROPOMI is mainly related to the differences in overpass time. This north-south dependency is much less significant in the comparison to MODIS data, as MODIS and TROPOMI overpass

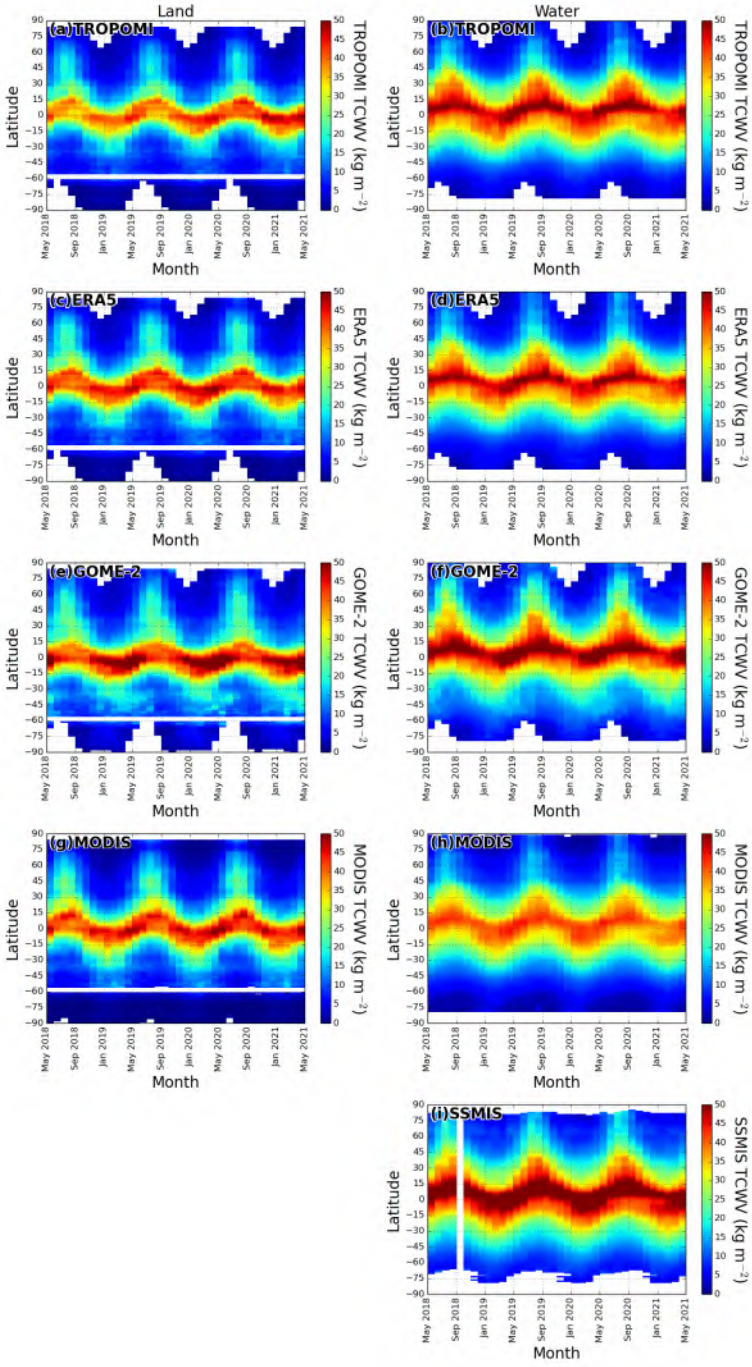

Figure 9: Monthly zonal average if TCWV from TROPOMI (1st row), ERA5 (2nd row), GOME-2 (3th row), MODIS (4th row), and SSMIS (5th row). Data are separated for observations over land (left column) and water (right column).

roughly at the same time. Compared to MODIS, TROPOMI measures lower TCWV over land and higher values over water. The discrepancies (dry bias over land and wet bias over water) are more significant over tropics and subtropics. The dry bias in the comparison to SSMIS observations over water is rather homogeneous (2 - 3 kg m^{-2}) with only slightly stronger dry bias in the tropics (15° S - 15° N).

Table 5: Summary of zonal mean and the corrsponding $1\,\sigma$ standard deviation of TCWV for all data sets at different latitude bands.

Latitude	Zonal mean and standard deviation of TCWV ($\mathrm{kg\,m^{-2}}$)				
	Land				
	TROPOMI	ERA5	GOME-2	MODIS	SSMIS
90°S - 60°S	2.38 ± 1.87	2.35 ± 1.94	4.32 ± 2.68	1.05 ± 1.15	–
60°S - 30°S	9.84 ± 3.19	10.87 ± 3.56	13.75 ± 3.65	11.56 ± 4.33	–
30°S - 0°	25.77 ± 11.66	28.08 ± 11.95	32.08 ± 13.22	28.93 ± 11.81	–
0° - 30°N	24.58 ± 10.80	26.69 ± 11.38	25.86 ± 11.37	27.57 ± 11.68	–
30°N - 60°N	9.42 ± 5.40	10.68 ± 6.02	11.53 ± 6.07	11.1 ± 6.43	–
60°N - 90°N	5.42 ± 3.39	6.2 ± 3.97	7.33 ± 4.08	4.93 ± 4.27	–
Latitude	Water				
	TROPOMI	ERA5	GOME-2	MODIS	SSMIS
90°S - 60°S	4.61 ± 1.54	4.78 ± 1.46	6.44 ± 2.41	3.58 ± 1.61	7.76 ± 1.43
60°S - 30°S	13.08 ± 5.51	12.24 ± 5.01	14.54 ± 4.18	11.98 ± 5.10	16.02 ± 5.64
30°S - 0°	33.41 ± 7.59	32.01 ± 7.99	31.68 ± 9.16	30.76 ± 6.95	37.30 ± 9.13
0° - 30°N	37.78 ± 8.95	36.39 ± 9.22	38.76 ± 10.10	33.33 ± 7.37	41.71 ± 10.36
30°N - 60°N	15.85 ± 8.46	15.18 ± 7.83	18.17 ± 8.71	14.56 ± 6.53	19.25 ± 8.26
60°N - 90°N	7.35 ± 3.76	8.05 ± 4.01	9.87 ± 5.24	6.6 ± 3.95	10.18 ± 4.32

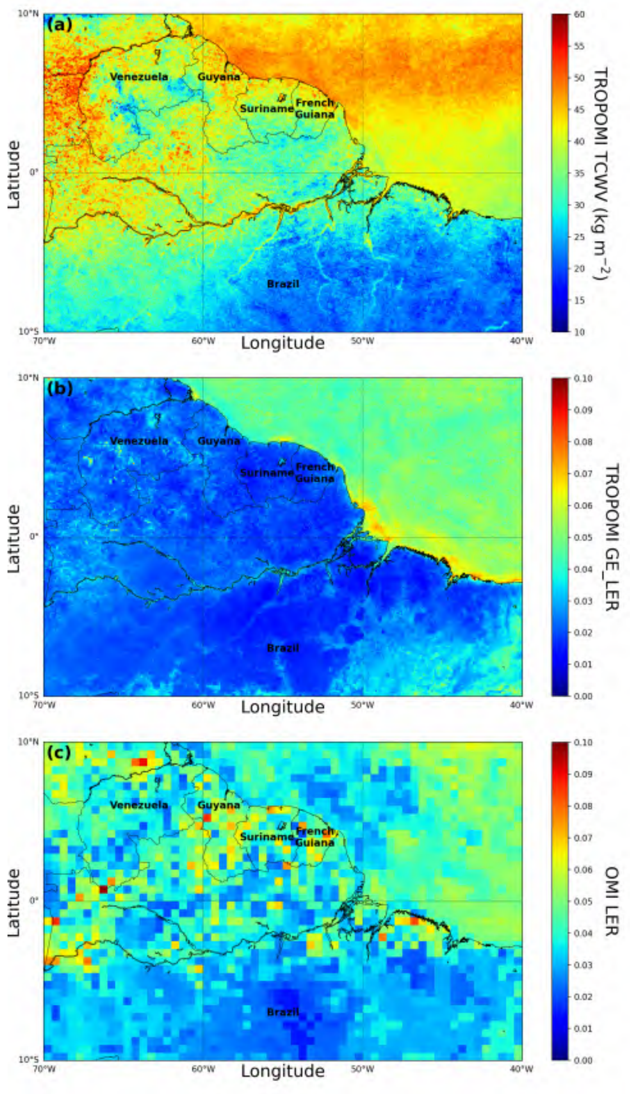

Figure 10: (a) Monthly averaged TCWV over northeast South America derived from TROPOMI observations in July 2019. (b) TROPOMI monthly averaged GE_LER and (c) OMI monthly minimum albedo climatology.

5. Fine scale features of water vapour

Fine scale features of water vapour can be observed from UVN space sensors with the significant enhancement of spatial resolution of TROPOMI. As the satellite ground pixels are not fully overlapped with each other for measurements within a certain period, i.e., the repeat cycle of the satellite orbit, this feature can be used to resample the data in a spatial resolution higher than the original satellite ground pixel when producing monthly average maps. This technique has been used to generate high resolution satellite maps for local and regional studies (Wenig et al., 2008; Chan et al., 2012, 2015). In order to exploit the full resolution of TROPOMI, we have gridded the TROPOMI TCWV data in a much finer resolution of $0.01° \times 0.01°$. The data filtering and gridding follows the description in Section 3.4. Figure 10a shows the monthly averaged TROPOMI TCWV over the northeast part of South America in July 2019. Some dynamical features of water vapour can be observed from the monthly averaged map. Enhanced water vapour columns can be seen not only over the main stream of the Amazon river, but also over smaller branches, e.g., Xingu, Tapajós and Madeira Rivers. Lower water vapour columns are also observed over the mountain areas at the borders among Venezuela, Guyana and Brazil. To make sure the fine scale structures measured are not artifacts caused by the input surface albedo, we have plotted the surface albedo data used in the retrieval in Figure 10b. Surface albedo derived from OMI is shown in Figure 10c for reference. The TROPOMI albedo is in resolution of $0.1° \times 0.1°$, while the OMI albedo is is in much coarser resolution of $0.5° \times 0.5°$. Albedo from TROPOMI observations over the main stream of Amazon River is slightly higher than its surroundings. However, some of the smaller branches, i.e., Xingu River, does not show up in the albedo map. Satellite measurement sensitivity is higher over surface with higher albedo, and results in higher air mass factors. As the spectral retrieval of slant column is independent to surface albedo, increase of air mass factor would results lower vertical columns. However, TCWV observed by TROPOMI over rivers are still higher than its surroundings which implies that the enhancement of TCWV is actually related to the increase of water vapour. The example of fine scale structures of water vapour demonstrated here indicates that the enhanced spatial resolution of TROPOMI data is useful not only for studies on global scale, but also for climate studies in local and regional scales.

6. Summary and conclusion

We presented the total column water vapour (TCWV) retrieval algorithm developed for the TROPOspheric Monitoring Instrument (TROPOMI) observations in the visible blue spectral band being developed and validated in the framework of the Sentinel 5 Precursor Product Algorithm Laboratory (S5P-PAL) project from the European Space Agency (ESA). The TROPOMI TCWV algorithm was based on the GOME-2 TCWV retrieval with optimization on the spectral fit, air mass factor calculations, and a new approach to retrieve surface properties from TROPOMI observations. The TROPOMI TCWV retrieval features a dynamic a priori profile algorithm, making it independent from profile information from a chemistry transport model. This feature avoids the model errors propagating to the satellite retrieval, or bias due to updates of model version. This makes it a better option for the processing of an independent long-term climate record.

The developed TCWV retrieval is applied to TROPOMI obsevations from May 2018 to May 2021. The TCWV results are validated by comparing to ERA5 reanalysis data, GOME-2, MODIS, and SSMIS satellite observations. TCWV derived from TROPOMI observations show very good spatio-temporal consistency with the other data sets, with a Pearson correlation coefficient (R) ranging from 0.96 to 0.99. The mean bias between TROPOMI and ERA5 data is -1.24 $\mathrm{kg\,m^{-2}}$ for measurements over land and 0.73 $\mathrm{kg\,m^{-2}}$ for measurements over water. The comparison to MODIS observations show similar results with small dry bias of 1.51,$\mathrm{kg\,m^{-2}}$ for measurements over land and a small wet bias of 1.25 $\mathrm{kg\,m^{-2}}$ for measurements over water. Slightly larger dry bias of 1.98 $\mathrm{kg\,m^{-2}}$ for measurements over land and 1.74 $\mathrm{kg\,m^{-2}}$ for measurements over water are found when compared to GOME-2 obserations. Compared to SSMIS data over water, TROPOMI observations are bias low by 3.25 $\mathrm{kg\,m^{-2}}$. The agreements to other data sets are slightly better in summer of the Northern Hemisphere compared to that of winter. The small discrepancies found between TROPOMI and reference data sets are related to the differences in measurement technique, measurement time, surface albedo issues, as well as cloud and aerosol contamination. Validation of TROPOMI TCWV against ground based observations, i.e., Global Positioning System (GPS), sun-photometer, and radiosonde measurements, will be addressed in separate studies. In addition, we have demonstrated that fine scale water vapour structures can be observed by TROPOMI over the Amazon basin, indicating the data set will also be useful for local and regional climate studies. The algorithm presented in this paper could be used for generating the operational ESA/EU TCWV products from TROPOMI/Sentinel-5 Precursor and will be the baseline for the future AC-SAF TCWV products from the Copernicus missions Sentinel-4 and Sentinel-5.

Acknowledgements

The work described in this paper is supported by European Space Agency (ESA) within the framework of Sentinel 5 Precursor Product Algorithm Laboratory (S5P-PAL) and the German Aerospace Center (DLR) programmatic research. Thanks to EU/ESA/KNMI/DLR for providing the TROPOMI L1b data (`https://scihub.copernicus.eu/`), AC-SAF for providing the GOME-2 TCWV products (`https://acsaf.org/`), ECMWF for providing the ERA5 reanalysis data (`https://cds.climate.copernicus.eu/`), NASA for providing the MODIS (`https://neo.gsfc.nasa.gov/`) and SSMIS (`https://ghrc.nsstc.nasa.gov/`) data.

References

Anderson, G.P., Clough, S.A., Kneizys, F., Chetwynd, J.H., Shettle, E.P.. AFGL atmospheric constituent profiles (0.120 km). Technical Report; U.S. Air Force Geophysics Laboratory, Optical Physics Division; 1986. URL: `https://apps.dtic.mil/sti/pdfs/ADA175173.pdf`.

Antón, M., Loyola, D., Román, R., Vömel, H.. Validation of GOME-2/MetOp-A total water vapour column using reference radiosonde data from the GRUAN network. Atmospheric Measurement Techniques 2015;8(3):1135–1145. doi:`10.5194/amt-8-1135-2015`.

Bauer, P., Schlüssel, P.. Rainfall, total water, ice water, and water vapor over sea from polarized microwave simulations and special sensor microwave/imager data. Journal of Geophysical Research: Atmospheres 1993;98(D11):20737–20759. doi:10.1029/93JD01577.

Bellomo, K., Clement, A., Mauritsen, T., Rädel, G., Stevens, B.. Simulating the role of subtropical stratocumulus clouds in driving pacific climate variability. Journal of Climate 2014;27(13):5119–5131. doi:10.1175/JCLI-D-13-00548.1.

Bernhard, G., Arola, A., Dahlback, A., Fioletov, V., Heikkilä, A., Johnsen, B., Koskela, T., Lakkala, K., Svendby, T., Tamminen, J.. Comparison of OMI UV observations with ground-based measurements at high northern latitudes. Atmospheric Chemistry and Physics 2015;15(13):7391–7412. doi:10.5194/acp-15-7391-2015.

Boersma, K.F., Eskes, H.J., Brinksma, E.J.. Error analysis for tropospheric NO_2 retrieval from space. Journal of Geophysical Research: Atmospheres 2004;109(D4). doi:10.1029/2003JD003962.

Borger, C., Beirle, S., Dörner, S., Sihler, H., Wagner, T.. Total column water vapour retrieval from S-5P/TROPOMI in the visible blue spectral range. Atmospheric Measurement Techniques 2020;13(5):2751–2783. doi:10.5194/amt-13-2751-2020.

Boucher, O., Randall, D., Artaxo, P., Bretherton, C., Feingold, G., Forster, P., Kerminen, V.M., Kondo, Y., Liao, H., Lohmann, U., Rasch, P., Satheesh, S., Sherwood, S., Stevens, B., Zhang, X.. Clouds and Aerosols; Cambridge, United Kingdom and New York, NY, USA: Cambridge University Press. p. 571–658. URL: www.climatechange2013.org. doi:10.1017/CBO9781107415324.016.

Bovensmann, H., Burrows, J.P., Buchwitz, M., Frerick, J., Noël, S., Rozanov, V.V., Chance, K.V., Goede, A.P.H.. SCIAMACHY: Mission objectives and measurement modes. Journal of the Atmospheric Sciences 1999;56(2):127 – 150. doi:10.1175/1520-0469(1999)056<0127:SMOAMM>2.0.CO;2.

Brion, J., Chakir, A., Charbonnier, J., Daumont, D., Parisse, C., Malicet, J.. Absorption spectra measurements for the ozone molecule in the 350-830 nm region. Journal of Atmospheric Chemistry 1998;30(2):291–299. doi:10.1023/A:1006036924364.

Brown, P.T., Li, W., Jiang, J.H., Su, H.. Unforced surface air temperature variability and its contrasting relationship with the anomalous toa energy flux at local and global spatial scales. Journal of Climate 2016;29(3):925–940. doi:10.1175/JCLI-D-15-0384.1.

Burrows, J.P., Weber, M., Buchwitz, M., Rozanov, V., Ladstätter-Weißenmayer, A., Richter, A., DeBeek, R., Hoogen, R., Bramstedt, K., Eichmann, K.U., Eisinger, M., Perner, D.. The global ozone monitoring experiment (GOME): Mission concept and first scientific results. Journal of the Atmospheric Sciences 1999;56(2):151 – 175. doi:10.1175/1520-0469(1999)056<0151:TGOMEG>2.0.CO;2.

Callies, J., Corpaccioli, E., Eisinger, M., Hahne, A., Lefebvre, A.. GOME-2-metop's second-generation sensor for operational ozone monitoring. ESA bulletin 2000;102:28–36. URL: https://www.esa.int/esapub/bulletin/bullet102/Callies102.pdf.

Chan, K., Hartl, A., Lam, Y., Xie, P., Liu, W., Cheung, H., Lampel, J., Pöhler, D., Li, A., Xu, J., Zhou, H., Ning, Z., Wenig, M.. Observations of tropospheric NO_2 using ground based MAX-DOAS and OMI measurements during the shanghai world expo 2010. Atmospheric Environment 2015;119:45–58. doi:10.1016/j.atmosenv.2015.08.041.

Chan, K.L., Pöhler, D., Kuhlmann, G., Hartl, A., Platt, U., Wenig, M.O.. NO_2 measurements in Hong Kong using LED based long path differential optical absorption spectroscopy. Atmospheric Measurement Techniques 2012;5(5):901–912. doi:10.5194/amt-5-901-2012.

Chan, K.L., Valks, P., Slijkhuis, S., Köhler, C., Loyola, D.. Total column water vapor retrieval for global ozone monitoring experience-2 (GOME-2) visible blue observations. Atmospheric Measurement Techniques 2020;13(8):4169–4193. doi:10.5194/amt-13-4169-2020.

Chance, K., Kurucz, R.. An improved high-resolution solar reference spectrum for earth's atmosphere measurements in the ultraviolet, visible, and near infrared. Journal of Quantitative Spectroscopy and Radiative Transfer 2010;111(9):1289–1295. doi:10.1016/j.jqsrt.2010.01.036.

Clough, S.A., Iacono, M.J.. Line-by-line calculation of atmospheric fluxes and cooling rates: 2. application to carbon dioxide, ozone, methane, nitrous oxide and the halocarbons. Journal of Geophysical Research: Atmospheres 1995;100(D8):16519–16535. doi:10.1029/95JD01386.

Colman, R.. A comparison of climate feedbacks in general circulation models. Climate Dynamics 2003;20(7):865–873. doi:10.1007/s00382-003-0310-z.

De Smedt, I., Theys, N., Yu, H., Danckaert, T., Lerot, C., Compernolle, S., Van Roozendael, M., Richter, A., Hilboll, A., Peters, E., Pedergnana, M., Loyola, D., Beirle, S., Wagner, T., Eskes, H., van Geffen, J., Boersma, K.F., Veefkind, P.. Algorithm theoretical baseline for formaldehyde retrievals from S5P TROPOMI and from the qa4ecv project. Atmospheric Measurement Techniques 2018;11(4):2395–2426. doi:10.5194/amt-11-2395-2018.

Efremenko, D.S., R., D.G.L., Hedelt, P., Spurr, R.J.D.. Volcanic SO_2 plume height retrieval from UV sensors using a full-physics inverse learning machine algorithm. International Journal of Remote Sensing 2017;38(sup1):1–27. doi:10.1080/01431161.2017.1348644.

Evan, A.T., Flamant, C., Lavaysse, C., Kocha, C., Saci, A.. Water vapor-forced greenhouse warming over the sahara desert and the recent recovery from the sahelian drought. Journal of Climate 2015;28(1):108 – 123. doi:10.1175/JCLI-D-14-00039.1.

Gao, B.C., Kaufman, Y.J.. Water vapor retrievals using moderate resolution imaging spectroradiometer (modis) near-infrared channels. Journal of Geophysical Research: Atmospheres 2003;108(D13). doi:10.1029/2002JD003023.

Grossi, M., Valks, P., Loyola, D., Aberle, B., Slijkhuis, S., Wagner, T., Beirle, S., Lang, R.. Total column water vapour measurements from gome-2 metop-a and metop-b. Atmospheric Measurement Techniques 2015;8(3):1111–1133. doi:10.5194/amt-8-1111-2015.

Hartmann, D., Klein-Tank, A., Rusticucci, M., Alexander, L., Brönnimann, S., Charabi, Y., Dentener, F., Dlugokencky, E., Easterling, D., Kaplan, A., Soden, B., Thorne, P., Wild, M., Zhai, P.. Observations: Atmosphere and Surface; Cambridge, United Kingdom and New York, NY, USA: Cambridge University Press. p. 159–254. URL: www.climatechange2013.org. doi:10.1017/CBO9781107415324.008.

Hedelt, P., Efremenko, D.S., Loyola, D.G., Spurr, R., Clarisse, L.. Sulfur dioxide layer height retrieval from Sentinel-5 Precursor/TROPOMI using FP_ILM. Atmospheric Measurement Techniques 2019;12(10):5503–5517. doi:10.5194/amt-12-5503-2019.

Hersbach, H., Bell, B., Berrisford, P., Hirahara, S., Horányi, A., Muñoz Sabater, J., Nicolas, J., Peubey, C., Radu, R., Schepers, D., Simmons, A., Soci, C., Abdalla, S., Abellan, X., Balsamo, G., Bechtold, P., Biavati, G., Bidlot, J., Bonavita, M., De Chiara, G., Dahlgren, P., Dee, D., Diamantakis, M., Dragani, R., Flemming, J., Forbes, R., Fuentes, M., Geer, A., Haimberger, L., Healy, S., Hogan, R.J., Hólm, E., Janisková, M., Keeley, S., Laloyaux, P., Lopez, P., Lupu, C., Radnoti, G., de Rosnay, P., Rozum, I., Vamborg, F., Villaume, S., Thépaut, J.N.. The era5 global reanalysis. Quarterly Journal of the Royal Meteorological Society 2020;146(730):1999–2049. doi:10.1002/qj.3803.

Hodnebrog, Ø., Myhre, G., Samset, B.H., Alterskjær, K., Andrews, T., Boucher, O., Faluvegi, G., Fläschner, D., Forster, P.M., Kasoar, M., Kirkevåg, A., Lamarque, J.F., Olivié, D., Richardson, T.B., Shawki, D., Shindell, D., Shine, K.P., Stier, P., Takemura, T., Voulgarakis, A., Watson-Parris, D.. Water vapour adjustments and responses differ between climate drivers. Atmospheric Chemistry and Physics 2019;19(20):12887–12899. doi:10.5194/acp-19-12887-2019.

Kalakoski, N., Kujanpää, J., Sofieva, V., Tamminen, J., Grossi, M., Valks, P.. Validation of GOME-2/Metop total column water vapour with ground-based and in situ measurements. Atmospheric Measurement Techniques 2016;9(4):1533–1544. doi:10.5194/amt-9-1533-2016.

Kaufman, Y.J., Gao, B... Remote sensing of water vapor in the near IR from EOS/MODIS. IEEE Transactions on Geoscience and Remote Sensing 1992;30(5):871–884. doi:10.1109/36.175321.

Kiehl, J.T., Trenberth, K.E.. Earth's annual global mean energy budget. Bulletin of the American Meteorological Society 1997;78(2):197–208. doi:10.1175/1520-0477(1997)078<0197:EAGMEB>2.0.CO;2.

King, M.D., Kaufman, Y.J., Menzel, W.P., Tanre, D.. Remote sensing of cloud, aerosol, and water vapor properties from the moderate resolution imaging spectrometer (modis). IEEE Transactions on Geoscience and Remote Sensing 1992;30(1):2–27. doi:10.1109/36.124212.

Klaes, K.D., Cohen, M., Buhler, Y., Schlüssel, P., Munro, R., Luntama, J.P., von Engeln, A., Clérigh, E.Ó., Bonekamp, H., Ackermann, J., Schmetz, J.. An introduction to the EUMETSAT polar system. Bulletin of the American Meteorological Society 2007;88(7):1085 – 1096. doi:10.1175/BAMS-88-7-1085.

Kleipool, Q., Ludewig, A., Babić, L., Bartstra, R., Braak, R., Dierssen, W., Dewitte, P.J., Kenter, P., Landzaat, R., Leloux, J., Loots, E., Meijering, P., van der Plas, E., Rozemeijer, N., Schepers, D., Schiavini, D., Smeets, J., Vacanti, G., Vonk, F., Veefkind, P.. Pre-launch calibration results of the TROPOMI payload on-board the sentinel-5 precursor satellite. Atmospheric Measurement Techniques 2018;11(12):6439–6479. doi:10.5194/amt-11-6439-2018.

Kleipool, Q.L., Dobber, M.R., de Haan, J.F., Levelt, P.F.. Earth surface reflectance climatology from 3 years of OMI data. Journal of Geophysical Research: Atmospheres 2008;113(D18). doi:10.1029/2008JD010290.

Lavers, D.A., Ralph, F.M., Waliser, D.E., Gershunov, A., Dettinger, M.D.. Climate change intensification of horizontal water vapor transport in cmip5. Geophysical Research Letters 2015;42(13):5617–5625. doi:10.1002/2015GL064672.

Levelt, P., Van den Oord, G.H.J., Dobber, M., Malkki, A., Visser, H., de Vries, J., Stammes, P., Lundell, J., Saari, H.. The ozone monitoring instrument. Geoscience and Remote Sensing, IEEE Transactions on 2006;44(5):1093–1101. doi:10.1109/TGRS.2006.872333.

Li, Z., Fielding, E.J., Cross, P., Muller, J.P.. Interferometric synthetic aperture radar atmospheric correction: Medium resolution imaging spectrometer and advanced synthetic aperture radar integration. Geophysical Research Letters 2006;33(6). doi:10.1029/2005GL025299.

Liu, J., Liang, H., Sun, Z., Zhou, X.. Validation of the moderate-resolution imaging spectroradiometer precipitable water vapor product using measurements from GPS on the tibetan plateau. Journal of Geophysical Research: Atmospheres 2006;111(D14). doi:10.1029/2005JD007028.

Liu, S., Valks, P., Pinardi, G., Xu, J., Chan, K.L., Argyrouli, A., Lutz, R., Beirle, S., Khorsandi, E., Baier, F., Huijnen, V., Bais, A., Donner, S., Dörner, S., Gratsea, M., Hendrick, F., Karagkiozidis, D., Lange, K., Piters, A.J.M., Remmers, J., Richter, A., Van Roozendael, M., Wagner, T., Wenig, M., Loyola, D.G.. An improved tropospheric NO_2 column retrieval algorithm for TROPOMI over Europe. Atmospheric Measurement Techniques Discussions 2021;2021:1–43. doi:10.5194/amt-2021-39.

Loyola, D.G., Gimeno García, S., Lutz, R., Argyrouli, A., Romahn, F., Spurr, R.J.D., Pedergnana, M., Doicu, A., Molina García, V., Schüssler, O.. The operational cloud retrieval algorithms from TROPOMI on board sentinel-5 precursor. Atmospheric Measurement Techniques 2018;11(1):409–427. doi:10.5194/amt-11-409-2018.

Loyola, D.G., Pedergnana, M., Gimeno García, S.. Smart sampling and incremental function learning for very large high dimensional data. Neural Networks 2016;78:75–87. doi:10.1016/j.neunet.2015.09.001.

Loyola, D.G., Xu, J., Heue, K.P., Zimmer, W.. Applying FP_ILM to the retrieval of geometry-dependent effective lambertian equivalent reflectivity (GE_LER) daily maps from UVN satellite measurements. Atmospheric Measurement Techniques 2020;13(2):985–999. doi:10.5194/amt-13-985-2020.

Ludewig, A., Kleipool, Q., Bartstra, R., Landzaat, R., Leloux, J., Loots, E., Meijering, P., van der Plas, E., Rozemeijer, N., Vonk, F., Veefkind, P.. In-flight calibration results of the TROPOMI payload on board the Sentinel-5 Precursor satellite. Atmospheric Measurement Techniques 2020;13(7):3561–3580. doi:10.5194/amt-13-3561-2020.

Martin, R.V., Chance, K., Jacob, D.J., Kurosu, T.P., Spurr, R.J.D., Bucsela, E., Gleason, J.F., Palmer, P.I., Bey, I., Fiore, A.M., Li, Q., Yantosca, R.M., Koelemeijer, R.B.A.. An improved retrieval of tropospheric nitrogen dioxide from GOME. Journal of Geophysical Research: Atmospheres 2002;107(D20):ACH 9–1–ACH 9–21. doi:10.1029/2001JD001027.

Mukherjee, S., Joshi, P., Mukherjee, S., Ghosh, A., Garg, R., Mukhopadhyay, A.. Evaluation of vertical accuracy of open source digital elevation model (DEM). International Journal of Applied Earth Observation and Geoinformation 2013;21:205–217. doi:10.1016/j.jag.2012.09.004.

Munro, R., Lang, R., Klaes, D., Poli, G., Retscher, C., Lindstrot, R., Huckle, R., Lacan, A., Grzegorski, M., Holdak, A., Kokhanovsky, A., Livschitz, J., Eisinger, M.. The GOME-2 instrument on the metop series of satellites: instrument design, calibration, and level 1 data processing – an overview. Atmospheric Measurement Techniques 2016;9(3):1279–1301. doi:10.5194/amt-9-1279-2016.

Noël, S., Buchwitz, M., Bovensmann, H., Hoogen, R., Burrows, J.P.. Atmospheric water vapor amounts retrieved from GOME satellite data. Geophysical Research Letters 1999;26(13):1841–1844. doi:10.1029/1999GL900437.

Noël, S., Buchwitz, M., Burrows, J.P.. First retrieval of global water vapour column amounts from SCIAMACHY measurements. Atmospheric Chemistry and Physics 2004;4(1):111–125. doi:10.5194/acp-4-111-2004.

Palmer, P.I., Jacob, D.J., Chance, K., Martin, R.V., Spurr, R.J.D., Kurosu, T.P., Bey, I., Yantosca, R., Fiore, A., Li, Q.. Air mass factor formulation for spectroscopic measurements from satellites: Application to formaldehyde retrievals from the global ozone monitoring experiment. Journal of Geophysical Research: Atmospheres 2001;106(D13):14539–14550. doi:10.1029/2000JD900772.

Platt, U., Stutz, J.. Differential optical absorption spectroscopy - principles and applications. Springer, 2008. doi:10.1007/978-3-540-75776-4_6.

Pope, R.M., Fry, E.S.. Absorption spectrum (380-700 nm) of pure water. ii. integrating cavity measurements. Appl Opt 1997;36(33):8710–8723. doi:10.1364/AO.36.008710.

Pougatchev, N., August, T., Calbet, X., Hultberg, T., Oduleye, O., Schlüssel, P., Stiller, B., Germain, K.S., Bingham, G.. Iasi temperature and water vapor retrievals – error assessment and validation. Atmospheric Chemistry and Physics 2009;9(17):6453–6458. doi:10.5194/acp-9-6453-2009.

Prasad, A.K., Singh, R.P.. Validation of MODIS Terra, AIRS, NCEP/DOE AMIP-II reanalysis-2, and AERONET sun photometer derived integrated precipitable water vapor using ground-based GPS receivers over india. Journal of Geophysical Research: Atmospheres 2009;114(D5). doi:10.1029/2008JD011230.

Román, R., Antón, M., Cachorro, V., Loyola, D., de Galisteo, J.O., de Frutos, A., Romero-Campos, P.. Comparison of total water vapor column from GOME-2 on MetOp-A against ground-based GPS measurements at the Iberian Peninsula. Science of The Total Environment 2015;533:317 – 328. doi:10.1016/j.scitotenv.2015.06.124.

Rothman, L.S., Gordon, I.E., Barbe, A., Benner, D.C., Bernath, P.F., Birk, M., Boudon, V., Brown, L.R., Campargue, A., Champion, J.P., Chance, K., Coudert, L.H., Dana, V., Devi, V.M., Fally, S., Flaud, J.M., Gamache, R.R., Goldman, A., Jacquemart, D., Kleiner, I., Lacome, N., Lafferty, W.J., Mandin, J.Y., Massie, S.T., Mikhailenko, S.N., Miller, C.E., Moazzen-Ahmadi, N., Naumenko, O.V., Nikitin, A., Orphal, J., Perevalov, V.I., Perrin, A., Predoi-Cross, A., Rinsland, C.P., Rotger, M., Šimečkovă, M., Smith, M.A.H., Sung, K., Tashkun, S.A., Tennyson, J., Toth, R.A., Vandaele, A.C., Auwera, J.V.. The HITRAN 2008 molecular spectroscopic database. Journal of Quantitative Spectroscopy and Radiative Transfer 2009;110(9¡V10):533–572. doi:10.1016/j.jqsrt.2009.02.013.

Salomonson, V.V., Barnes, W.L., Maymon, P.W., Montgomery, H.E., Ostrow, H.. Modis: advanced facility instrument for studies of the earth as a system. IEEE Transactions on Geoscience and Remote Sensing 1989;27(2):145–153. doi:10.1109/36.20292.

Schneider, T., O'Gorman, P.A., Levine, X.J.. Water vapor and the dynamics of climate changes. Reviews of Geophysics 2010;48(3). doi:10.1029/2009RG000302.

Soden, B.J., Held, I.M.. An assessment of climate feedbacks in coupled ocean – atmosphere models. Journal of Climate 2006;19(14):3354–3360. doi:10.1175/JCLI3799.1.

Soden, B.J., Jackson, D.L., Ramaswamy, V., Schwarzkopf, M.D., Huang, X.. The radiative signature of upper tropospheric moistening. Science 2005;310(5749):841–844. doi:10.1126/science.1115602.

Solomon, S., Schmeltekopf, A.L., Sanders, R.W.. On the interpretation of zenith sky absorption measurements. Journal of Geophysical Research: Atmospheres 1987;92(D7):8311–8319. doi:10.1029/JD092iD07p08311.

Spurr, R.. LIDORT and VLIDORT: Linearized pseudo-spherical scalar and vector discrete ordinate radiative transfer models for use in remote sensing retrieval problems; Berlin, Heidelberg: Springer Berlin Heidelberg. p. 229–275. doi:10.1007/978-3-540-48546-9_7.

Stephens, G.L., Jackson, D.L., Bates, J.J.. A comparison of ssm/i and tovs column water vapor data over the global oceans. Meteorology and Atmospheric Physics 1994;54(1):183–201. doi:10.1007/BF01030059.

Stutz, J., Platt, U.. Numerical analysis and estimation of the statistical error of differential optical absorption spectroscopy measurements with least-squares methods. Applied Optic 1996;35(30):6041–6053. doi:10.1364/AO.35.006041.

Thalman, R., Volkamer, R.. Temperature dependent absorption cross-sections of o_2-o_2 collision pairs between 340 and 630 nm and at atmospherically relevant pressure. Phys Chem Chem Phys 2013;15:15371–15381. doi:10.1039/C3CP50968K.

Theys, N., De Smedt, I., Yu, H., Danckaert, T., van Gent, J., Hörmann, C., Wagner, T., Hedelt, P., Bauer, H., Romahn, F., Pedergnana, M., Loyola, D., Van Roozendael, M.. Sulfur dioxide retrievals from TROPOMI onboard sentinel-5 precursor: algorithm theoretical basis. Atmospheric Measurement Techniques 2017;10(1):119–153. doi:10.5194/amt-10-119-2017.

Trenberth, K.E., Stepaniak, D.P.. Covariability of components of poleward atmospheric energy transports on seasonal and interannual timescales. Journal of Climate 2003;16(22):3691–3705. doi:10.1175/1520-0442(2003)016<3691:COCOPA>2.0.CO;2.

Vandaele, A.C., Hermans, C., Fally, S., Carleer, M., Colin, R., Merienne, M.F., Jenouvrier, A., Coquart, B.. High-resolution fourier transform measurement of the NO_2 visible and near-infrared absorption cross sections: Temperature and pressure effects. Journal of Geophysical Research: Atmospheres 2002;107(D18):ACH 3–1–ACH 3–12. doi:10.1029/2001JD000971.

Vaquero-Martínez, J., Antón, M., de Galisteo, J.P.O., Cachorro, V.E., Álvarez-Zapatero, P., Román, R., Loyola, D., ao Costa, M.J., Wang, H., Abad, G.G., Noël, S.. Inter-comparison of integrated water vapor from satellite instruments using reference GPS data at the Iberian Peninsula. Remote Sensing of Environment 2018;204:729 – 740. doi:10.1016/j.rse.2017.09.028.

Veefkind, J., Aben, I., McMullan, K., Förster, H., de Vries, J., Otter, G., Claas, J., Eskes, H., de Haan, J., Kleipool, Q., van Weele, M., Hasekamp, O., Hoogeveen, R., Landgraf, J., Snel, R., Tol, P., Ingmann, P., Voors, R., Kruizinga, B., Vink, R., Visser, H., Levelt, P.. TROPOMI on the ESA Sentinel-5 Precursor: A GMES mission for global observations of the atmospheric composition for climate, air quality and ozone layer applications. Remote Sensing of Environment 2012;120:70 – 83. doi:10.1016/j.rse.2011.09.027.

Wagner, T., Beirle, S., Grzegorski, M., Platt, U.. Global trends (1996-2003) of total column precipitable water observed by global ozone monitoring experiment (GOME) on ERS-2 and their relation to near-surface temperature. Journal of Geophysical Research: Atmospheres 2006;111(D12). doi:10.1029/2005JD006523.

Wagner, T., Beirle, S., Sihler, H., Mies, K.. A feasibility study for the retrieval of the total column precipitable water vapour from satellite observations in the blue spectral range. Atmospheric Measurement Techniques 2013;6(10):2593–2605. doi:10.5194/amt-6-2593-2013.

Wang, H., Gonzalez Abad, G., Liu, X., Chance, K.. Validation and update of OMI total column water vapor product. Atmospheric Chemistry and Physics 2016;16(17):11379–11393. doi:10.5194/acp-16-11379-2016.

Wang, H., Liu, X., Chance, K., González Abad, G., Chan Miller, C.. Water vapor retrieval from OMI visible spectra. Atmospheric Measurement Techniques 2014;7(6):1901–1913. doi:10.5194/amt-7-1901-2014.

Wang, H., Souri, A.H., González Abad, G., Liu, X., Chance, K.. Ozone monitoring instrument (OMI) total column water vapor version 4 validation and applications. Atmospheric Measurement Techniques 2019;12(9):5183–5199. doi:10.5194/amt-12-5183-2019.

Wenig, M.O., Cede, A.M., Bucsela, E.J., Celarier, E.A., Boersma, K.F., Veefkind, J.P., Brinksma, E.J., Gleason, J.F., Herman, J.R.. Validation of OMI tropospheric NO_2 column densities using direct-sun mode brewer measurements at NASA goddard space flight center. Journal of Geophysical Research: Atmospheres 2008;113(D16). doi:10.1029/2007JD008988.

Wentz, F.J.. A well-calibrated ocean algorithm for special sensor microwave / imager. Journal of Geophysical Research: Oceans 1997;102(C4):8703–8718. doi:10.1029/96JC01751.

Wentz, F.J.. A 17-yr climate record of environmental parameters derived from the tropical rainfall measuring mission (TRMM) microwave imager. Journal of Climate 2015;28(17):6882–6902. doi:10.1175/JCLI-D-15-0155.1.

Xu, J., Schüssler, O., Rodriguez, D.G.L., Romahn, F., Doicu, A.. A novel ozone profile shape retrieval using full-physics inverse learning machine (FP-ILM). IEEE Journal of Selected Topics in Applied Earth Observations and Remote Sensing 2017;10(12):5442–5457. doi:10.1109/JSTARS.2017.2740168.

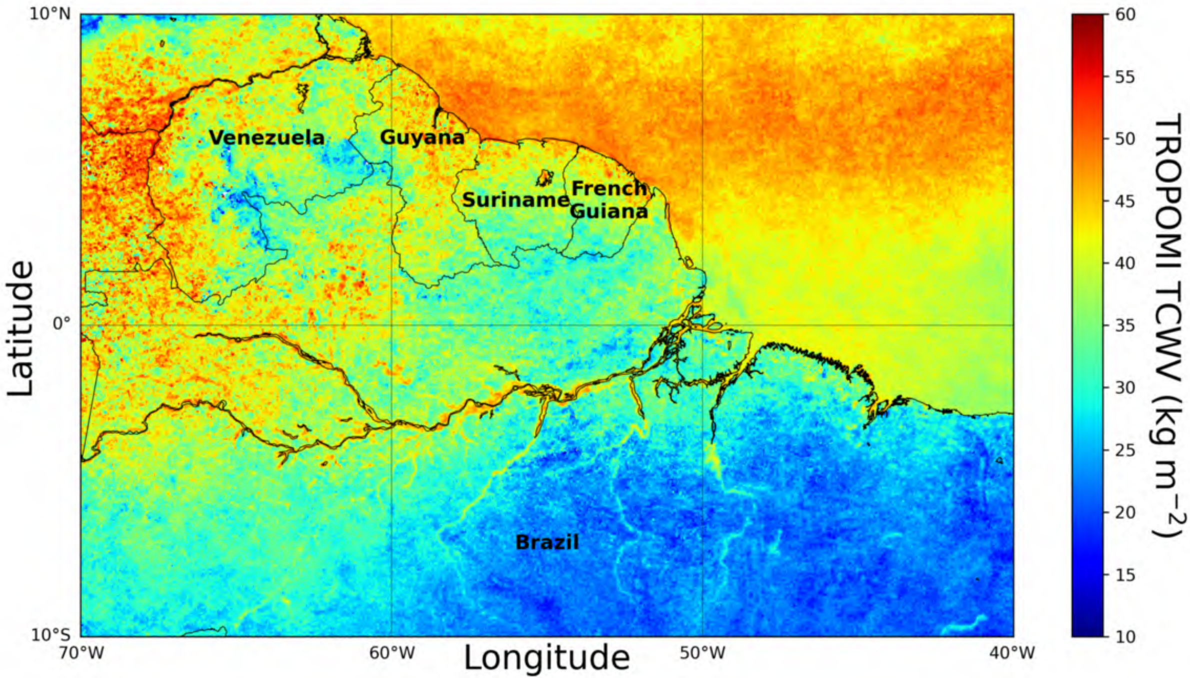

10°N
0°
10°S
70°W
60°W
50°W
40°W
Latitude
Longitude
Venezuela
Guyana
Suriname
French
Guiana
Brazil
TROPOMI TCWV (kg m^{-2})
60
55
50
45
40
35
30
25
20
15
10